



# Auto-ignition characteristics of coal-based naphtha

Jinzhou Li <sup>a</sup>, An Lu <sup>b,c</sup>, Yu Xie <sup>a</sup>, Junfeng Yang <sup>a,\*</sup>, Chunhua Zhang <sup>c</sup>

<sup>a</sup> School of Mechanical Engineering, University of Leeds, Leeds LS2 9JT, United Kingdom

<sup>b</sup> School of Mechanical Engineering, Shanghai Jiao Tong University (SJTU), Shanghai 200240, PR China

<sup>c</sup> School of Automobile, Chang'an University, Xi'an 710064, PR China

## HIGHLIGHTS

- Measured the auto-ignition delay time of coal-based naphtha.
- Evaluated the knock tendency, culminating in the presentation of a knock map.
- A  $\xi$ - $\epsilon$  detonation peninsula for analyzing the evolution of ignition modes.
- An evidences on the chemical reactions governing the transition of detonation.

## ARTICLE INFO

### Keywords:

Coal-based naphtha  
Ignition delay time  
Knock  
Detonation peninsula  
Optical RCM

## ABSTRACT

Coal-based naphtha features a low Octane number and is a promising fuel as potential energy supplements for advanced compression ignition engines where the auto-ignition dominates the combustion process. However, its auto-ignition characteristics including ignition delay times (IDTs), knocking propensity have not been well studied yet. In the present work, the Leeds optical Rapid Compression Machine (RCM) equipped with simultaneous pressure acquisition and high-speed photography was implemented to study the IDTs and knock properties of coal-based naphtha over a wide range of temperatures (640–900 K), pressures (1.0–2.0 MPa) and equivalence ratios (0.5–1.5). A three-component surrogate model with detailed oxidation kinetics has been developed to predict the IDTs, excitation time and heat release rate for coal-based naphtha. Both pressure traces and combustion luminosity images indicated that the onsets of knock and super-knock are related to the initiation of ‘detonation-like hot-spot’ before the arrival of reaction wave. A knock map derived from the measured pressure traces showed the knock and super-knock tendency to occur at high temperature and rich equivalence ratio regime. Moreover, the Bradley's  $\xi$ - $\epsilon$  diagram was adopted to classify and interpret the evolution of ignition modes of coal-based naphtha in RCM. In this context,  $\xi$  represents ratio of acoustic velocity,  $a$ , into autoignitive velocity,  $u_a$ . The  $\epsilon$  quantifies the rapidity of heat release in a hot spot and is defined as  $\frac{r_{\text{max}}}{\Delta t_{\text{cr}}}$ . The combination of super-knock pressure oscillation, detonation images and  $\xi$ - $\epsilon$  parameters all provided the evidence that the super-knock is related to the transition of detonation.

## 1. Introduction

Transport sector contributed approximately 21.7% of global greenhouse gas (GHG) emissions in 2022 [1], principally from petroleum derived liquid fuels that are particularly difficult to decarbonise. Due to energy density challenges in developing pure electric propulsion systems for heavy goods, shipping and aviation sectors, societal reliance on liquid fuels is likely to continue beyond the near term. It is therefore crucial to explore alternative liquid fuels with lower lifetime GHG emissions compared to fossil fuels. Naphtha featuring a low Research

Octane Number (RON) and Motor Octane Number (MON) has been proposed as a potential energy vector for engines operating under advanced ignition modes, such as homogeneous charge compression ignition (HCCI), partially premixed compression ignition, and gasoline compression ignition simultaneously improve the thermal efficiency and reduce the carbon emissions per kW power output [2]. From the perspective of life cycle assessment, the coal-based naphtha as an intermediate product in the coal refining process, streamlines the procedure of coal refining process including reforming and catalytic cracking. Consequently, this leads to a decrease in GHG emissions when compared to coal-derived diesel and coal-based gasoline. Moreover, the

\* Corresponding author.

E-mail address: [J.Yang@leeds.ac.uk](mailto:J.Yang@leeds.ac.uk) (J. Yang).

<https://doi.org/10.1016/j.apenergy.2024.122768>

Received 14 October 2023; Received in revised form 17 January 2024; Accepted 26 January 2024

Available online 3 February 2024

0306-2619/© 2024 The Author(s). Published by Elsevier Ltd. This is an open access article under the CC BY license (<http://creativecommons.org/licenses/by/4.0/>).

Nomenclature		Abbreviation	
$a$	acoustic velocity (m/s)	AI	Auto-ignition
$u_a$	theoretical auto-ignitive velocity (m/s)	BMF	Burned Mass Fraction
$T$	temperature (K)	CFR	Cooperative Fuel Research
$T_{eoc}$	end of compression temperature (K)	CI	Compression Ignition
$T_{ai}$	auto-ignition temperature during explosion (K)	EOC	End of Compression
$T_i$	initial temperature (K)	FACE	Fuels for Advanced Combustion Engines
$t_{50}$	timeframe for the final 50% of pressure rise (ms)	GCDHA	Gas Chromatography-Detailed Hydrocarbon Analysis
$r_0$	hot spot radius (mm)	GHG	Global Greenhouse Gas
$P$	pressure (MPa)	HCCI	Homogeneous Charge Compression Ignition
$P_{eoc}$	end of compression pressure (MPa)	HRR	Heat Release Rate
$P_{ai}$	auto-ignition pressure during compression (MPa)	HSRN	Haltermann Straight Run Naphtha
$P_i$	initial pressure (MPa)	IDTs	Ignition delay times
$\Delta P_{max}$	maximum value of pressure oscillation (MPa)	KI	Knock Intensity
$\tau_e$	chemical excitation time ( $\mu$ s)	LLNL	Lawrence Livermore National Laboratory
$\tau_i$	ignition delay time (ms)	MON	Motor Octane Number
<b>Greek symbols</b>		MPCI	Multiple Premixed Compression Ignition
$\gamma$	the ratio of specific heats	NTC	Negative Temperature Coefficient
$\phi$	equivalence ratio	PRF	Primary Reference Fuel
$\xi$	ratio of $u_a/a$	PLIF	Planar Laser-Induced Fluorescence
$\varepsilon$	ratio of $\frac{r_0}{a\tau_e}$	RCM	Rapid Compression Machine
		RON	Research Octane Number

coal-based naphtha does not contain aromatic hydrocarbons and olefins. The study of Albert et al. [3] from gasoline-powered vehicles reported that the reducing olefins led to lower emissions of  $\text{NO}_x$ , while reducing aromatics resulted in decreased HC and CO emissions. Therefore, coal-based naphtha presents a significant advantage in terms of improving engine efficiency and reducing exhaust emissions.

The auto-ignition (AI) properties of naphtha are important in HCCI engines that are compression ignited, and determine the overall engine power, emission, and thermal efficiency. Therefore, the IDTs and knock onset of naphtha have been studied in RCM, shock-tubes and engines, and the corresponding surrogate fuel models have been proposed and tested. Mitakos et al. [4] investigated the IDTs of petroleum-based naphtha and three primary reference fuels (PRFs) in RCM, and a good agreement between the measured IDTs data and empirical three-stage Arrhenius IDTs model was reported. Javed et al. [5] measured the IDTs of light naphtha in RCM and shock tube over a wide range of temperatures (640–1250 K), equivalence ratio (0.5, 1.0, 1.5) and pressure (2.0 and 4.0 MPa). Alabbad et al. [6] measured the IDTs of Haltermann straight-run naphtha (HSRN) using a shock tube and a rapid compression machine, comparing it with models from formulated surrogates across various pressures, temperatures, and equivalence ratios. The study revealed that the PRF surrogate effectively represents HSRN under high-load conditions, while a multi-component surrogate is needed for low engine loads. Zhong et al. [7] explored the pyrolysis and oxidation behaviors of a light naphtha fuel and its formulated surrogate blend (a three-component surrogate containing 64.2 mol% isopentane, 21.0 mol% *n*-hexane and 14.8 mol% methyl cyclopentane) in a jet-stirred reactor over a wide range of equivalence ratio and temperature. The comparison indicated that the mole fraction profiles of hydrogen and C1 - C3 hydrocarbons in the surrogate fuel is close to the light naphtha. Wang et al. [8] investigated the impact of injection pressure on the combustion and emission characteristics of heavy naphtha in Multiple Premixed Compression Ignition (MPCI) mode, revealing that higher injection pressures favor the thermal efficiency of heavy naphtha combustion. Celebi et al. [9] investigated the utilization of light naphtha in an HCCI engine by analyzing the engine load, fuel consumption, in-cylinder pressure and emissions, surprisingly almost zero NO emission was observed for all HCCI operating conditions indicating that naphtha is an environmentally friendly fuel.

Though plenty of data and surrogate models for petroleum-derived naphtha have been reported, the available data for coal-based naphtha is dearth. Only very recently, Lu et al. [10] investigated the knock properties of coal-based naphtha in a lean HCCI engine ( $\phi \sim 0.2$ ) through analyzing the in-cylinder pressure using artificial intelligence method. They reported the coal-base naphtha is a promising fuel for HCCI engine, as it can operate smoothly at a compression ratio 17:1. Since coal-based naphtha has completely different compositions (almost nil cycloalkanes) compared to that of petroleum-derived naphtha, the existing ignition data and surrogates developed for petroleum-based naphtha are not applicable for coal-based naphtha. Therefore, the auto-ignition characteristics need to be examined for coal-based naphtha carefully.

Measurements of IDTs in engines would be very complex due to the continually changing conditions and the complex flow fields. Thus, in order to enhance fundamental understanding and interpretation, measurements are usually conducted under controllable conditions in relatively simple devices, e.g. combustion vessels, and flow reactors for low-pressure conditions, RCM and shock tubes for high-pressure conditions more closely related to HCCI engines. The RCM is more appropriate for IDTs in the millisecond and greater range and shock tube is more suitable for shorter IDTs [11]. RCMs have been exploited for nearly a century and are continually being improved [12]. The most important contribution to the gas motion in RCMs arises during compression from the roll-up vortices, which can be controlled via creviced pistons to achieve the homogeneity temperature field [13]. Hence, the IDTs of coal-based naphtha were measured using Leeds RCM with creviced piston which has been successfully employed and validated over many years of experience in characterising transportation fuels.

Beyond the IDTs dependence on  $T$  and  $P$ , a second fundamental of AI is a fuel's propensity for localized initiation in inhomogeneous regions. Significant over-pressures and pressure waves can be generated from AI of inhomogeneous hotspots, which might be either damaging or beneficial, according to intensity. Hotspots generated AI phenomena play role in knock and other unwanted AI events in engines and are the main obstacle of increasing the engine compression ratio to improve the thermal efficiency. Different outcomes can follow from a sequence of auto-ignitions, generated from local gradients in temperature and/or chemical concentrations, e.g. due to turbulent mixing. The

fundamentals of such processes and the qualitative dependence on the magnitude of the spatial gradient of local  $\tau_i$  values are established [14]. If the speed of the AI front is comparable to the acoustic speed the role of diffusion is limited and the heat release drives pressure waves. In turn, the speed of the AI front is strongly coupled to and in feed-back with the pressure wave generation and steepening. The coupling can lead to the formation of shock waves, and in extremis the formation of a violent detonation wave. Theory and simulations of AI waves generated from localized gradients in temperature [15–18] have quantified the mechanisms and the different possible regimes of feedback between pressure wave and AI times. These theoretical ideas have received experimental confirmation, notably in [19] where a modified optical RCM device with a stratification of temperature resulted in the observation of such AI fronts. And this thermal gradient was further characterized for methane-air mixture in an optical RCM using toluene planar laser-induced fluorescence (PLIF) thermometry [20].

The RCM experiments study of Pan et al. [21] and Wang et al. [22] reported that the knock is associated with the end-gas auto-ignition before the reaction front arrival and following with pressure oscillation. More recently, Büttgen et al. [23], Wang et al. [24], and Liu et al. [25] have employed an optical RCM equipped with a high-speed camera to investigate the ignition phenomena in ethanol, methanol, and isooctane, particularly focusing on the evolution of autoignition front speed. Additionally, Pan et al. [26] used an optical RCM to explore the impact of turbulence on pre-ignition, finding that while turbulent mixing with colder boundary layers tends to prolong the IDTs, pre-ignition phenomena continue to be observable. And the evolution speeds of AI fronts are directly linked to the onset of DDT, i.e. knocking. However, all previous studies focused on the high-octane-rating fuels, e.g. *i*-octane (RON 100), methanol (RON ~108) and ethanol (RON ~108), which feature a low-propensity to knock. And their AI properties are less indicative for coal-based naphtha (RON 54 and MON 45). It is therefore necessary to investigate the propensity for localized initiation of hot-spots for coal-based naphtha and identify its knocking boundary using dimensionless groups. Understanding the knock characteristics of coal-based naphtha is necessary for its application in compression ignition (CI) engines with high compression ratios (>15).

In light of the above considerations, the aim of this study is to measure the IDTs of coal-based naphtha and understand its ignition and knock properties through an optical visualization RCM with pressure measurements. The IDTs of coal-based naphtha are derived from the pressure traces measured through the Leeds RCM along with a three-component surrogate model. The high-speed imaging is employed to record the reaction wave initiation, propagation, and transition to detonation, which shows the evolution of the hot-spot induced reaction wave, especially for knocking cases. Moreover, the Bradley's  $\xi$ - $\epsilon$  diagram [27,28] is adopted to quantify the ignition modes including subsonic auto-ignition, developing detonation and thermal explosion of naphtha along with the increasing compression temperature. The chemical kinetics analysis indicates that the chain-branching reaction  $\text{H}_2\text{O} + \text{M} < \geq \text{H} + \text{OH} + \text{M}$  dominates the heat release in all ignition modes. Finally, a knock map is proposed to show the regime of normal auto-ignition, knock and super-knock with temperature and equivalence ratio. The detonation peninsula using dimensionless groups,  $\xi$ - $\epsilon$ , can guide the knock-free operating for CI engines powered by coal-based naphtha.

## 2. Methodology

### 2.1. The specifications of coal-based naphtha and surrogate model

The generic term naphtha refers to a flammable liquid hydrocarbon mixture. It should be noted that the composition of the naphtha varies depending on the feedstock (petroleum or coal) and the manufacturing method (catalytic reforming or destructive distillation) used in their production, which will affect the fuel's properties. Table 1 provides partial specifications (including chemical formula, RON, MON, low

**Table 1**  
Specifications of coal-based naphtha used in the RCM experimental studies [10].

Properties	Coal-based naphtha
Average chemical formula	$\text{C}_{6.971}\text{H}_{15.882}$
Research octane number (RON)	54
Motor octane number (MON)	45
Lower heating value (MJ/kg)	45.73
Density at 20 °C ( $\text{g}/\text{cm}^3$ )	0.67
Kinematic viscosity at 20 °C ( $\text{mm}^2/\text{s}$ )	0.56
Sulfur content (mg/kg)	<1
Nitrogen content (mg/kg)	<1
Water content (mg/kg)	356

heating value and density, etc.) for coal-based naphtha that were produced by China National Energy Group Ningxia Coal Industry Co. Ltd. and used in the RCM experiments discussed in this work. The RON and MON values presented in Table 1 were measured adhering to specified Chinese National Standards. For the RON value measurement, China National Energy Group Ningxia Coal Industry Co. Ltd. utilized a Cooperative Fuel Research (CFR) engine, conducting the assessment in alignment with the standard GB/T 5487–2011. Conversely, the MON value was measured by UFA-Tech Co., Ltd. (Shanghai), employing a CFR engine and adhering to the standard GB/T 503–2016. Both the RON and MON values were measured using a CFR engine operating at a flexible compression ratio. In each method, the detonation meter reading of the naphtha fuel sample was measured. For the RON value, interpolation was based on the readings of two reference fuels, *n*-heptane and *i*-octane, with known RON values. Similarly, the MON value was interpolated using the same reference fuels but correlating with their known MON values.

The composition of coal-based naphtha has been analyzed using the Gas Chromatography-Detailed Hydrocarbon Analysis (GCDHA) method, and the detailed results are provided in [29]. Briefly, the main components of coal-based naphtha are *n*-paraffins, isoparaffins and naphthene accounting for 20.18%, 75.64%, 3.78% (by mass), respectively. The chemical formula of coal-based naphtha ( $\text{C}_{6.971}\text{H}_{15.882}$ ) were calculated by taking the sum of the property of each component from GCDHA multiplied by its molar fraction. Moreover, the coal-based naphtha does not contain aromatic hydrocarbons and olefins, which offers a significant benefit in reducing the exhaust emissions such as HC, CO and  $\text{NO}_x$  as previously discussed.

Following the blending rule of Knop et al. [30], a three-components surrogate model (*n*-hexane, *n*- $\text{C}_6\text{H}_{14}$ : *i*-octane, *i*- $\text{C}_8\text{H}_{18}$ : *i*-heptane, *i*- $\text{C}_7\text{H}_{16}$  62.4:32.5:5.1 by mol%) for the coal-based naphtha was proposed to match the RON and H/C ratio in this study. This blending rule has been also successfully employed in [29] for the modelling of laminar burning velocity of coal-based naphtha. The oxidation kinetics of constituent components of surrogate model are available in the detailed gasoline chemical kinetics [31] by Lawrence Livermore National Laboratory (LLNL), and the Fuels for Advanced Combustion Engines (FACE) gasoline kinetics [32]. The LLNL gasoline kinetics were validated through the measured IDTs data of stoichiometric PRF, 1-hexene and toluene from an RCM and shock tubes covering a wide range of pressure (0.3–5.5 MPa) and temperature (640–1200 K). Similarly, the FACE kinetics were validated with the ignition experiments from shock tubes and a RCM at pressure from 2.0 to 4.0 MPa, temperature from 650 to 1270 K and equivalence ratios from 0.5 to 1. The detailed combustion kinetics of 3-component surrogate model based on LLNL gasoline kinetics and FACE gasoline kinetics were then employed for predicting the IDTs and the excitation time for coal-based naphtha/air mixtures under closed homogeneous batch reactor conditions using the CHEMFIN-PRO software [33]. The predicted excitation time,  $\tau_e$ , and ignition delay time,  $\tau_i$  were used to calculate dimensionless groups ( $\xi$ - $\epsilon$ ) in detonation peninsula discussed in Section 3.5. Table 2 shows the comparison of chemical formula, RON, H/C ratio and average molecular weight of coal-based naphtha and its surrogate model.

**Table 2**  
Comparison of coal-based naphtha and its surrogate.

	Coal-based naphtha	3-component surrogate
Average chemical formula	C <sub>6.97</sub> H <sub>15.882</sub>	C <sub>6.701</sub> H <sub>15.402</sub>
RON	54	54
MON	45	–
H/C ratio	2.278	2.298
Average molecular weight	99.742	95.814

## 2.2. Experimental apparatus

All experiments discussed in the present work were conducted using the Leeds optical RCM that has been successfully employed and validated over many years of experience for characterising the ignition properties of transportation fuels. The present configuration of Leeds RCM shown in Fig. 1 consists of combustion chamber, hydraulic damped chamber, pneumatic driving, displacement laser system and the mixing chamber. It employs a creviced piston to reduce the effects of aerodynamic mixing during the compression process and is configured for a wide range of pressures (1.0–3.0 MPa) and temperatures (600–1000 K) at the End of Compression (EOC). The end of the chamber, the ‘cylinder head’, is fitted with an optically flat, fused silica window (69 mm diameter × 40 mm thick). This window permits a full view of the chamber cross-section for imaging the scattered laser light, or natural light emission for on-line combustion species analysis.

The mixing chamber, connecting pipes, and piston cylinder are preheated to a temperature between 350 and 360 K using multiple band-heaters. The specific pre-heating temperature is strategically set to align with the end of compression pressure. To ensure a uniform temperature distribution, the components are heated for a duration of five hours prior to conducting the experiments. The preheating process plays a crucial role in ensuring consistent and reliable experimental conditions by facilitating the complete vaporization of all liquid fuels and preventing the condensation of fuel as it transitions into the combustion chamber.

A vacuum pump was employed to vacuum both mixing and combustion chamber. Prior to the mixture preparation, the mixing chamber is vacuumed into an absolute pressure <10 mbar, followed by filling it with dry compressed air up to 2 bar absolute pressure. This vacuum and

purge process was repeated twice to effectively eliminate any residual substances from previous mixtures. Subsequently, the coal-based naphtha, oxygen, and dilution gases (Ar, N<sub>2</sub>, and CO<sub>2</sub>) were combined using the partial pressure method in a 1.8 L stainless steel mixing chamber. The mixture was then allowed to rest for two hours to ensure homogeneity. Given that no significant changes in the IDTs measurements were observed under the studied conditions within a waiting time of 1–1.5 h, a two-hour period appears sufficient to achieve mixture homogeneity. Similarly, for each experiment, the combustion chamber underwent the same procedure. It was initially evacuated to an absolute pressure of <10 mbar and then filled with dry compressed air up to 7 bar absolute pressure. This vacuum and purge process was also repeated twice to effectively remove any residues from previous experiments. Following this, the mixtures from the mixing chamber were transferred into the combustion chamber, utilizing the pressure difference. The volume of the inlet mixtures was then determined using the partial pressure method.

The hydraulic oil is pumped into the damping chamber to the pressure of 4.0 MPa and this pressure holds the piston while the pneumatic driving reservoir was filled with the high-pressure driving air to 1.35 MPa pressure. The firing of RCM is controlled by a trigger which releasing the hydraulic oil pressure and the high-pressure driving air forces the piston forward, completing the compression in 18 ms. Notably, the  $t_{50}$  metric, representing the timeframe for the final 50% of pressure rise and crucial for characterising reaction kinetics during compression, is achieved within 1.9 ms. This efficient compression process heats and pressurizes the reactive mixtures to the EOC temperature  $T_{EOC}$ , and pressure  $P_{EOC}$ , within the combustion chamber. The remaining oil in the damped chamber serves to damp and hold the motion of piston as it enters the combustion chamber, preventing the piston from bouncing back once it reaches the end of compression position. The displacement of the piston during compression process was recorded by using a Keyence LK-G32 linear displacement laser system.

Fig. 2 provides the view of optical combustion chamber. It consists of a cylindrical combustion chamber with 45 mm diameter, a high strength quartz window with 69 mm visibility diameter 40 mm thickness to achieve full vision access. Certainly, compared to the metal head setup, the quartz window increases the heat loss during compression. However,

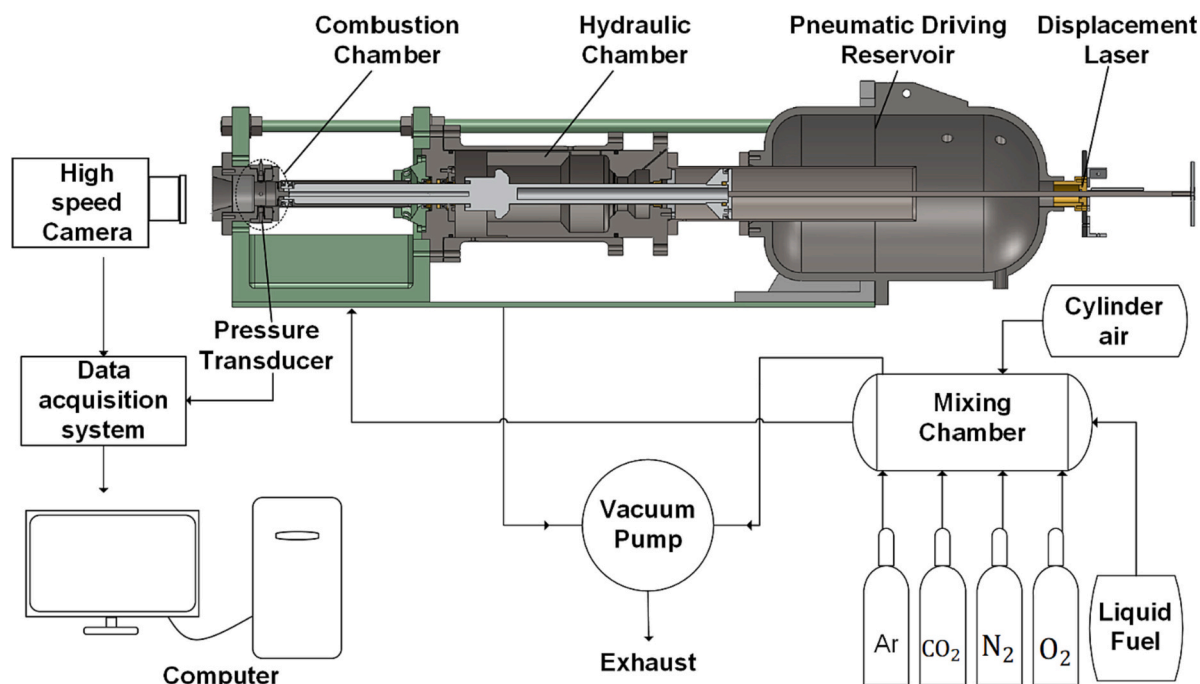


Fig. 1. The overall layout of the Leeds optical RCM Rig and high-speed imaging system.

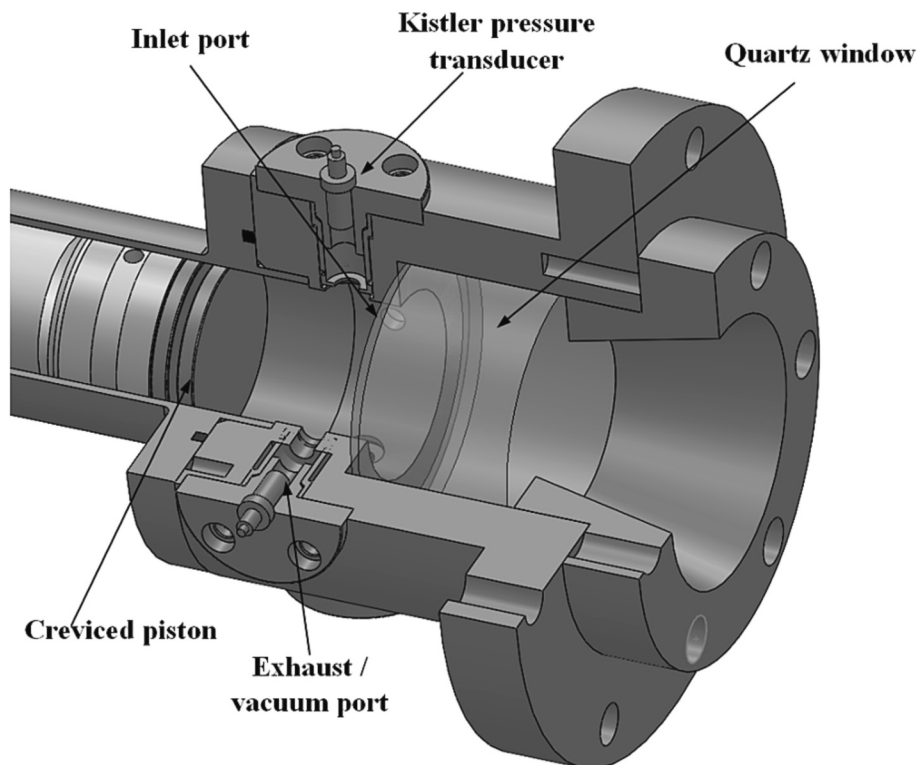


Fig. 2. The view of combustion chamber of Leeds optical RCM.

a comparison of the pressure traces from both setups indicates that these amounts of heat loss are not significant influences the results. A dynamic pressure transducer (Kistler 6045 A) was flush-mounted on the cylinder wall to record the in-cylinder pressure signal with a sampling rate of 100 kHz. The mixtures from the mixing chamber flush into the combustion chamber through the inlet port and after the explosion, the productions from combustion exhausted from the exhaust/vacuum port.

A monochrome high-speed CMOS camera (Photron Fastcam SA1.1) with a Tokina AT-X PRO lens with 2.8 aperture positioned immediately in front of the quartz window to record the radiations from the evolving reactions with two resolution setups  $256 \times 256$  and  $512 \times 512$  pixels. The framing rate was 67,500 frame per second (fps) for  $256 \times 256$  with pixel size of 0.176 mm/pixel and 20,000 fps for  $512 \times 512$  pixels with pixel size of 0.0879 mm/pixel. The shutter speed maintained at 14.81  $\mu$ s. The focal plan is focused on the piston front which located at the EOC position. The calibration work is performed by matching the pixel size and focal plan. A National Instruments BNC-2110 terminal block was utilized for control and data acquisition. This terminal block interfaces with the laser displacement system, pressure amplification system, and the camera trigger port. Upon the firing of the RCM, both the pressure transducer and laser displacement system were synchronized to trigger simultaneously. The camera itself was activated by the laser displacement signal, with timing set to initiate when the piston was 12 mm away from the EOC.

The MATLAB code [34] with command “imbinarize” using binarizing-thresholding technique [35] was used to define the reaction area characteristics. This method is widely used in [21,24–26] to post-process the images from RCM. The monochrome images were loaded by the MATLAB code to form the matrix of pixel numbers and binarized for a defined threshold. Those with an intensity higher than threshold were classed as burned mixture while lower than threshold as unburned mixture. The burned mass fraction (BMF) was defined as the number of pixels in the burned area over the total pixels of burned and unburned. The sample images showing the evolution of combustion-related luminosity images of coal-based naphtha from Leeds optical RCM are

presented top row in Fig. 3. The second row represents the post-processed binarized images derived from the binarizing-thresholding technique and the clearly white area represents the burned area. The time scale at the bottoms shows the times after the first observed reaction spot.

### 2.3. Experimental conditions

In general, the ignition properties of transportation fuels, e.g. IDTs, negative temperature coefficient (NTC) behavior, are determined by mixture strength (equivalence ratio,  $\phi$ ), the temperature ( $T_{eoc}$ ) and pressure ( $P_{eoc}$ ) at the EOC of RCM. To study the impact of these parameters on IDTs under different operating conditions, RCM experiments were conducted for 40 cases covering low- to intermediate-temperatures ( $T_{eoc} \in 640\text{--}900$  K) and lean-rich mixtures ( $\phi \in 0.5\text{--}1.5$ ) for coal-based naphtha at a fixed  $P_{eoc} = 2.0$  MPa. For the stoichiometric coal-based naphtha mixture, three different  $P_{eoc}$  values of 1.0, 1.5 and 2.0 MPa were selected. The experimental repeatability was checked through the five realizations at each experimental condition. Details of each experimental condition are providing in Table 3. Note that the end of compression temperature,  $T_{eoc}$  is calculated based on the adiabatic core hypothesis. This hypothesis assumed the compression process is rapid enough to achieve an adiabatic core gas with heat loss occurring only at the boundary layer.  $T_{eoc}$  is expressed as:

$$\frac{T_{eoc}}{T_i} = \left( \frac{P_{eoc}}{P_i} \right)^{\frac{\gamma-1}{\gamma}} \quad (1)$$

where,  $T_i$  is the initial temperature,  $P_i$  is the initial pressure and  $\gamma$  is the ratio of specific heats of the mixtures. The  $\gamma$  value for coal-based naphtha was ascertained by summing the  $\gamma$  values of its primary components, which were identified via GCDHA. The specific heat capacity of each component was then calculated based on the 5-order NASA polynomial equation. This approach was validated by correlating the results with  $P_{eoc}$ . The compression ratio and the initial pressure in the combustion cylinder determined  $P_{eoc}$  that was monitored and ensured by a dynamic

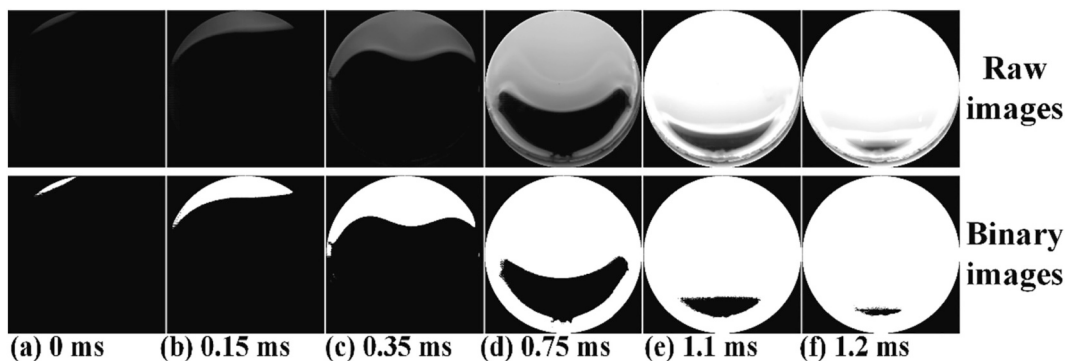


Fig. 3. Sample images showing combustion-related luminosity and binary from the rich coal-based naphtha/oxygen mixture ( $\phi = 1.2$ ) within Leeds optical RCM ( $T_{eoc} = 710$  K,  $P_{eoc} = 2.0$  MPa).

Table 3  
Experimental conditions for coal-naphtha combustion in Leeds optical RCM.

$\phi$	Mixture Composition Mole Fractions Layout (% by mole)					Thermodynamic target	
	Naphtha	Oxygen	Nitrogen	Argon	Carbon dioxide	$P_{eoc}$ [MPa]	$T_{eoc}$ [K]
0.5	0.92%	20.5%	0	0	78.4%	2.0	640
0.5	0.92%	20.5%	17.8%	0	60.6%	2.0	670
0.5	0.92%	20.5%	29.6%	0	48.7%	2.0	690
0.5	0.92%	20.5%	38.6%	0	39.8%	2.0	710
0.5	0.92%	20.5%	50.4%	0	27.9%	2.0	740
0.5	0.92%	20.5%	59.4%	0	18.9%	2.0	770
0.5	0.92%	20.5%	74.3%	4%	0	2.0	830
0.5	0.92%	20.5%	56.5%	21.8%	0	2.0	900
0.8	1.46%	20.5%	7.8%	0	70.1%	2.0	640
0.8	1.46%	20.5%	25.5%	0	52.3%	2.0	670
0.8	1.46%	20.5%	37.3%	0	40.5%	2.0	690
0.8	1.46%	20.5%	47.2%	0	30.6%	2.0	710
0.8	1.46%	20.5%	59%	0	18.9%	2.0	740
0.8	1.46%	20.5%	67%	0	10%	2.0	770
0.8	1.46%	20.5%	67%	10%	0	2.0	830
0.8	1.46%	20.5%	41.4%	36.4%	0	2.0	900
1	1.82%	20.5%	7.8%	0	70.1%	1.0, 1.5, 2.0	640
1	1.82%	20.5%	31.3%	0	46.3%	1.0, 1.5, 2.0	670
1	1.82%	20.5%	42.1%	0	35.5%	1.0, 1.5, 2.0	690
1	1.82%	20.5%	52%	0	25.6%	1.0, 1.5, 2.0	710
1	1.82%	20.5%	63.8%	0	13.8%	1.0, 1.5, 2.0	740
1	1.82%	20.5%	77.7%	0	0	1.0, 1.5, 2.0	770
1	1.82%	20.5%	56.9%	20.7%	0	1.0, 1.5, 2.0	830
1	1.82%	20.5%	31.4%	46.3%	0	1.0, 1.5, 2.0	900
1.2	2.18%	20.5%	13.6%	0	63.7%	2.0	640
1.2	2.18%	20.5%	37.1%	0	40.2%	2.0	670
1.2	2.18%	20.5%	47.8%	0	29.5%	2.0	690
1.2	2.18%	20.5%	56.7%	0	20.6%	2.0	710
1.2	2.18%	20.5%	69.4%	0	7.9%	2.0	740
1.2	2.18%	20.5%	72.7%	0	5%	2.0	770
1.2	2.18%	20.5%	47%	30.3%	0	2.0	830
1.2	2.18%	20.5%	20.6%	56.7%	0	2.0	900
1.5	2.71%	20.5%	21.3%	0	55.6%	2.0	640
1.5	2.71%	20.5%	44.7%	0	32.2%	2.0	670
1.5	2.71%	20.5%	55.4%	0	21.5%	2.0	690
1.5	2.71%	20.5%	65.2%	0	11.7%	2.0	710
1.5	2.71%	20.5%	76.8	0	0	2.0	740
1.5	2.71%	20.5%	62.3%	14.6%	0	2.0	770
1.5	2.71%	20.5%	32.1%	44.8%	0	2.0	830
1.5	2.71%	20.5%	5.8	71%	0	2.0	900

pressure transducer. For the purpose of comparison and validation, the *i*-octane (purity 99% by mass) and the *n*-heptane (purity 99% by mass) were tested under the stoichiometric condition with  $T_{eoc} \in 640\text{--}900$  K and  $P_{eoc} = 2.0$  MPa. The recorded time history of in-cylinder pressure was used to determine the IDTs of coal-based naphtha. The monochrome images for combustion-related luminosity were employed to determine the burned mass fraction assuming a cylindrical reaction wave propagates through the combustion chamber. The combination of pressure data and raw images enables the analysis of knock initiation. Furthermore, the knock map and detonation peninsula constructed using the dimensionless groups ( $\xi\text{-}\epsilon$ ) help identify the knock and detonation boundary of coal-based naphtha.

### 3. Results and discussion

#### 3.1. Typical pressure trace of coal-based naphtha

The dimensionless knock intensity (*KI*) defined as  $\Delta P_{max}/P_{eoc}$  is employed to categorize the ignition mode: the knocking-free is defined as the amplitude of pressure oscillation nearly equals to zero;  $KI \in (0.5\text{--}3)$  for knocking and  $KI \geq 3$  for super-knocking.  $\Delta P_{max}$  is the difference between maximum and minimum pressure oscillation and an example of  $\Delta P_{max}$  is shown in Fig. 4. The typical pressure traces of super-knock, knock and knock-free for naphtha/oxygen mixtures at  $P_{eoc} = 2$  MPa,  $T_{eoc} = 710\text{--}900$  K, are depicted in Fig. 4. As shown, the higher  $T_{eoc}$  ( $\geq 770$  K) tends to trigger the super-knock as indicated by the strong pressure oscillations ( $\Delta P_{max} \geq 6$  MPa) with knock intensity of 3. And the super-knock deteriorates to the normal knock as the stoichiometric naphtha becomes leaner ( $\phi = 0.8$ ). This is because the reactivity of naphtha/oxygen mixture increases as the temperature rises, while decreases as the mixture becomes leaner.

The RCM, in theory, is an ideal homogeneous reactor with multiple hotspots instantaneous thermal explosion. However, in practical RCMs, the non-uniform temperature distributions, turbulence-chemistry interaction, reaction during compression etc., lead to non-uniform ignition such as single hot spot propagation, pre-ignition and end-gas detonation. Bradley and coworkers [17,28] employed the Zeldovich hot spot temperature gradient theory [36] to categorize the auto-ignition development modes as deflagration, auto-ignition, detonation and thermal explosion. In line with this categorization, prior studies [21,22] have reported that the phenomenon of super-knock observed in RCM is attributed to the bouncing of detonation waves around the combustion chamber. These three different pressure traces in Fig. 4 must correspond to different auto-ignition development modes occurred in RCM.

For the purpose of comparison, the pressure traces of stoichiometric *i*-octane, *n*-heptane and naphtha are presented in Fig. 5 under the same initial condition,  $T_{eoc} = 710$  K,  $P_{eoc} = 2$  MPa. It is observed that under these conditions, both *i*-octane and naphtha exhibit knock-free

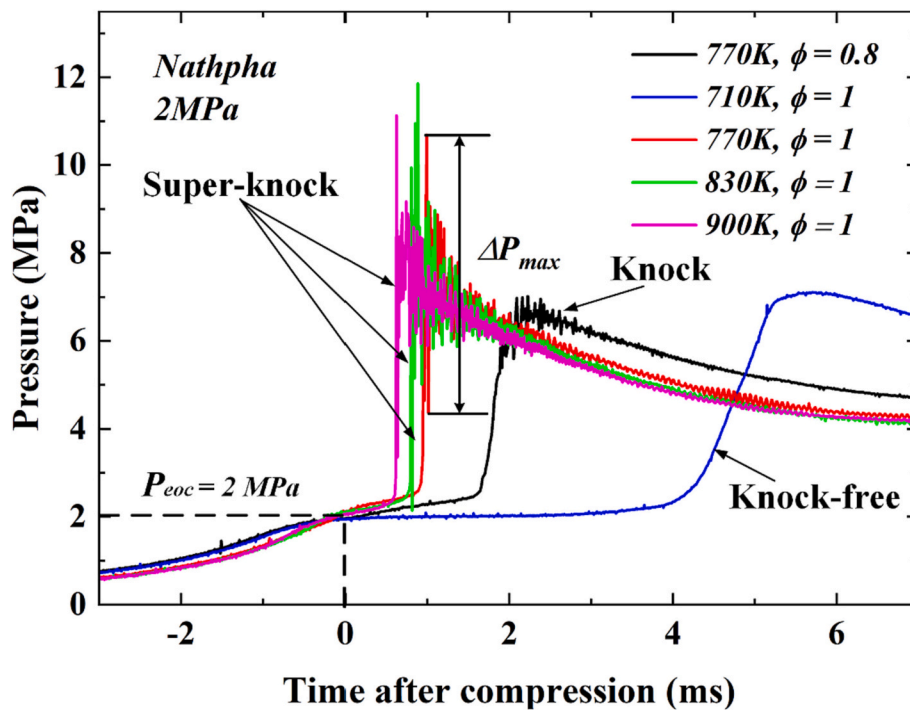


Fig. 4. Typical pressure traces of super-knock, knock and knock-free for naphtha/oxygen mixtures at  $P_{eoc} = 2.0$  MPa,  $T_{eoc} = 710$ – $900$  K in RCM.

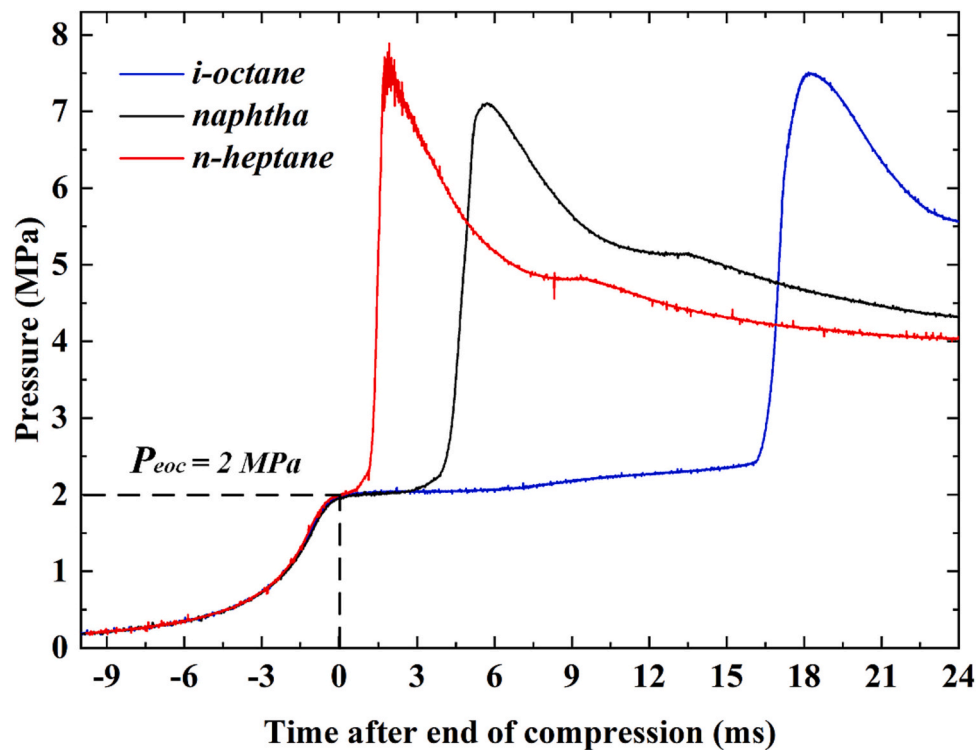


Fig. 5. Pressure traces of *i*-octane, coal-based naphtha, and *n*-heptane at  $P_{eoc} = 2.0$  MPa,  $T_{eoc} = 710$  K and  $\phi = 1$ .

combustion, whereas *n*-heptane demonstrates a knock combustion characteristic. The *n*-heptane (RON = 0) has the shortest  $\tau_i$  about 1.42 ms, then following with the coal-based naphtha (RON = 54) about 4.9 ms and the *i*-octane (RON = 100) with about 17 ms. The pressure traces in Fig. 5 re-assure that the RON of naphtha lies between those of *n*-heptane and *i*-octane.

### 3.2. IDTs of naphtha

Following the work of [37–39], the IDTs in this study, was defined as the time between the end of compression and the point at which the maximum gradient of the pressure rises ( $dP/dt$ ). Representative combustion pressure and its derivative used to determine the ignition delay are shown in Fig. 6.

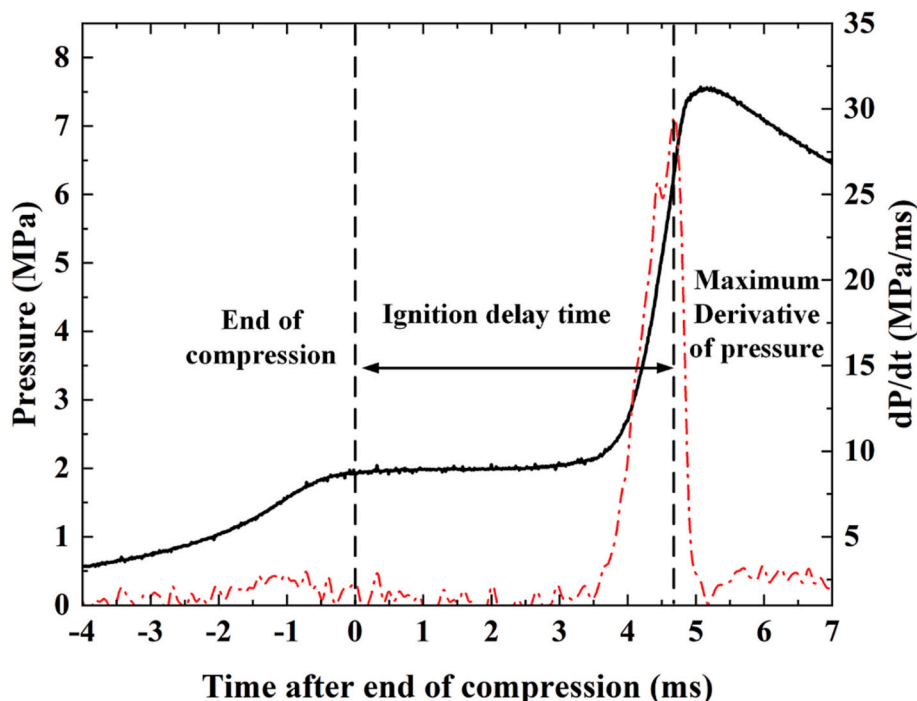


Fig. 6. The time history of combustion pressure (black solid line) and the derivative of pressure trace (red dashed line) for naphtha/oxygen mixtures at  $\phi = 1.2$ , 710 K and 2.0 MPa. (For interpretation of the references to colour in this figure legend, the reader is referred to the web version of this article.)

The measured and predicted IDTs,  $\tau_i$ , as a function of the inverse temperature  $1000/T$ , for coal-based naphtha are presented in Fig. 7 (a)–(f). Here  $T$  equals the end of compression temperature,  $T_{eoc}$ . The experimental results are indicated by filled symbols, solid lines denote the values predicted using the 3-component surrogate model based on the detailed LLNL gasoline mechanism, with dashed lines for the FACE mechanism.

The data cover the range of low to intermediate temperatures, 640–900 K, equivalence ratio 0.5–1.5, pressure 1.0–2.0 MPa. The standard deviation error bar was presented and defined as the square root of the variance, which is calculated by dividing the sum of squared deviations by the number of data points, 5, for each test condition. The stoichiometric naphtha/oxygen in Fig. 7 (f) exhibits apparent NTC behavior under the temperature range 740–830 K and 770–900 K for  $P_{eoc} = 1.0$  and 1.5 MPa respectively, where  $\tau_i$  increases with the increasing of temperature. The presence of the NTC regime is related to the oxidation of alkanes, which the developments of cool flames at temperature several hundred degrees lower than the minimum auto-ignition temperature decline the reactivity of the mixture in the NTC regime [40]. Meanwhile,  $\tau_i$  decreases as the pressure increases because the increasing of pressure enhances the reactivity of mixture. However, the NTC becomes less pronounced at higher pressure due to the increased stability of  $RO_2$  radical and radical  $H_2O_2$  decomposes faster [39]. Outside the NTC region,  $\tau_i$  decreases exponentially with decreasing temperature, so-called Arrhenius-like behavior that is consistent with the PRF blends [41] and light naphtha [5]. Figs. 7 (a)–(e) illustrate that  $\tau_i$  decreases from lean to stoichiometric conditions, while from stoichiometric to rich conditions,  $\tau_i$  exhibits minimal variation. In general, the measured  $\tau_i$  of naphtha lies between those of *i*-octane (RON = 100) and *n*-heptane (RON = 0) as expected in Fig. 7 (c).

In Fig. 7(f), the 3-component surrogate model from both LLNL and FACE mechanisms demonstrate nearly identical  $\tau_i$  values, aligning well with the measured data at 1.0 MPa. However, at 1.5 MPa, both mechanisms yield  $\tau_i$  higher than the measurements, although they correctly identify the NTC boundary. This trend of higher predicted values continues at 2.0 MPa. In the low temperature range of 640–740 K, the measured  $\tau_i$  of naphtha at 2 MPa closely matches the predictions. Yet, at

equivalence ratios of 1, 1.2, and 1.5, the predicted  $\tau_i$  values are approximately 1 ms higher than the measured data. Both mechanisms exhibit a consistent pattern of producing higher  $\tau_i$  values than measured, particularly evident in the significant NTC behavior at a pressure of 2.0 MPa across all equivalence ratios within the intermediate temperature range of 770–900 K. Additionally, as shown in Fig. 7 (c), for *i*-octane, the predictions align well with measurements at 640 K and 900 K, but the predicted values are higher in the NTC regime (710–830 K), despite accurately capturing the NTC boundary. The same figure also indicates that for both naphtha and *n*-heptane, the mechanisms tend to yield higher  $\tau_i$  values than measured, especially in the intermediate temperature range of 770 to 900 K.

The discrepancy between the measured and predicted  $\tau_i$  for naphtha in the intermediate temperature range of 770–900 K can be attributed to two main factors. Firstly, the reaction occurred during the compression process will lead to the measured  $\tau_i$  shorter than the ideal  $\tau_i$ . The previous study of Mohamed [42], Curran et al. [43] and Mittal et al. [44] indicated that high temperature and pressure conditions the chemical reaction during the compression has a significant effect on  $\tau_i$  particularly in the case of low octane fuels with short  $\tau_i$ . The compression duration in RCMs is typically within the range of 20 to 50 milliseconds and the reaction occurring during the compression phase in RCM experiments is an inherent aspect of the process and cannot be avoided [45]. Despite the inherent limitations that affect the accuracy of  $\tau_i$  measurements for naphtha, a global comparison of RCMs as detailed in [46] shows that the Leeds RCM has the fastest compression time. However, the  $\tau_i$  for naphtha at 2 MPa and  $T_{eoc}$  above 770 K are <2 ms. This presents a challenge as the  $t_{50} = 1.9$  ms of the Leeds RCM, though fast, is comparably lengthy for accurately measuring such short  $\tau_i$  durations.

The second factor might be attributed to the presence of radical initiation processes during the piston compression stroke, which may accelerate the development of the radical pool [47]. For fuels with high Octane rating (e.g. *i*-octane, RON = 100), the radical initiation process is weak. While, for highly reactive fuels such as *n*-heptane (RON = 0) and naphtha (RON = 54), the radical initiation process becomes strong, and leads to an increasing concentration of the radical species, which results in a marked effect on characteristic  $\tau_i$ , simply because The influence of

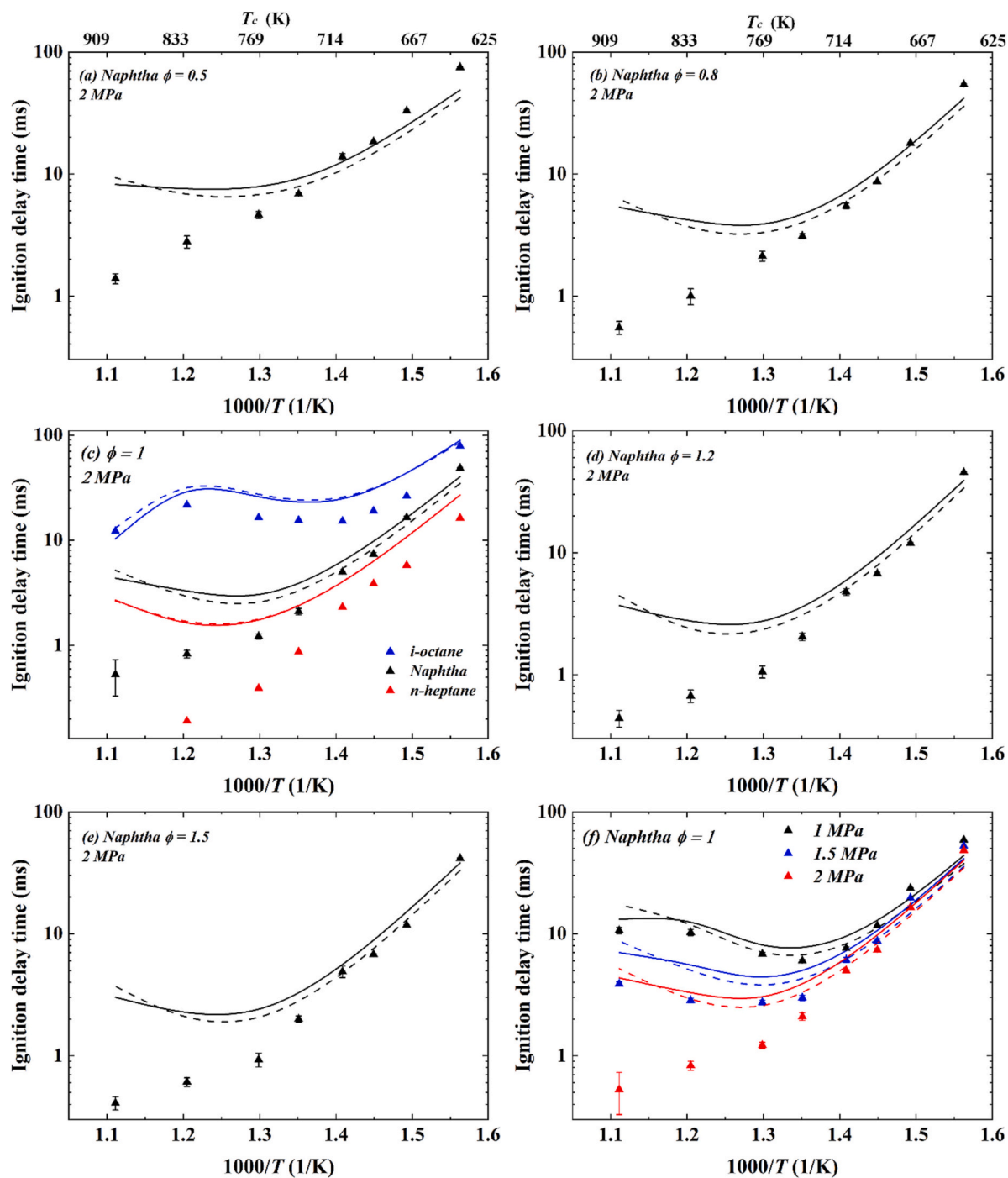


Fig. 7. Measured and predicted IDTs for: (a) naphtha at  $\phi = 0.5$ , 2.0 MPa, (b) naphtha at  $\phi = 0.8$ , 2.0 MPa, (c) naphtha, *i*-octane and *n*-heptane at  $\phi = 1.0$ , 2.0 MPa, (d) naphtha at  $\phi = 1.2$ , 2.0 MPa, (e) naphtha at  $\phi = 1.5$ , 2.0 MPa, (f) naphtha at  $\phi = 1.0$ , 1.0 MPa, 1.5 MPa and 2.0 MPa. Filled symbols: RCM measured data. Solid lines: LLNL gasoline kinetics [31]. Dashed lines: FACE gasoline kinetics [32]. Error bands are presenting for experiments.

pre-EOC reactivity is then manifested and become more influential at short  $\tau_i$  (under high pressure and high temperature conditions e.g. 2 MPa, 770–900 K) since the chemical induction processes have characteristic times that are comparable to the observed  $\tau_i$  at these conditions. Due to the nature of this behavior, it can cause inaccurate uniform  $\tau_i$  measurements by generating times much shorter than those predicted using kinetics model (via Chemkin-Pro) without accounting for the influence of pre-EOC reactivity. However, it is critical to note that as the  $T_{EOC}$  beyond 770 K at 2 MPa, the measured  $\tau_i$  fall below 1 ms, which is beyond the range of reliable measurement for the RCM.

### 3.3. Visualization of reaction wave propagation and burned mass fraction (BMF)

The pressure trace in RCM only provides quantitative analysis of ignition properties. To reveal the actual ignition mode underlying those different pressure traces, the RCM equipped with optical access was employed to provide information on the homogeneity of reaction, engine knock phenomena, hot-spot induced auto-ignition and transition to detonation. Previous studies employed optical RCMs for a better understanding on transition to detonation of *i*-octane [22], knock mechanism [21,48] and the ignition phenomenon of ethanol [23] and

methanol [24].

The monochrome image sequences in Fig. 8 are for stoichiometric naphtha/oxygen mixtures from the onset of auto-ignition until the 90% BMF under three different  $T_{eoc} = 640$  K, 670 K, 690 K, 710 K, 740 K and 770 K with an  $P_{eoc} = 2.0$  MPa. The minimum  $T_{eoc}$  for coal-based naphtha to auto-ignite is 640 K and the maximum safe operation  $T_{eoc}$  for the optical access is 770 K due to the destructive pressure wave induced by the knock. To enhance the contract ratio of burned to unburnt area, the Gamma value that quantifies the relationship between a pixel's numerical value and luminance was set as 0.4 for 640 K, while 0.5 for higher temperatures. The time zone in Fig. 8 started from the first observed ignition point from high-speed camera and ended at 90% BMF that was defined as the fraction of the number of pixels in the burned area over the total pixels of both burned and unburned. It is crucial to note that in the subplots (a) and (b) for BMF and pressure trace, the zero time is defined as the onset of autoignition, rather than the EOC time. For the case of  $T_{eoc} = 640$  K, two hot-spots (bright regions, also called onset of auto-ignition points) were presented simultaneously near both sides (left and right) of cylinder wall, and then propagated towards the centre of combustion chamber (as indicated by the red arrows in luminosity image Fig. 8 (b) of 640 K case). The whole combustion process from onset of ignition till 90% BMF took about 8.75 ms.

At higher  $T_{eoc}$  up to 770 K, similar propagation patterns were observed, with a single hot-spot near the cylinder wall. This hot-spot initiated at the top of the cylinder and gradually spread throughout the entire combustion chamber. Furthermore, a comparison of the BMF and pressure evolution indicates that both the reaction wave propagation speed and the burning rate increase significantly with  $T_{eoc}$ . In the pressure trace plot of Fig. 8(b), from  $T_{eoc} = 640$  K until 710 K, the pressure curves remain smooth throughout the combustion process, showing no evident pressure oscillations ( $\Delta P_{max} \approx 0$  MPa). This suggests that these conditions are knock-free and can be classified as deflagration mode and AI mode, respectively, according to [49]. The pressure oscillation was first observed at  $T_{eoc} = 740$  K with  $\Delta P_{max} \approx 1$  MPa at 0.25 ms indicating the knock onset. As the  $T_{eoc}$  reached 770 K, interestingly, a detonation-like ignition spot was initiated at the bottom of cylinder before the reactive wave reached it (see luminosity image Fig. 8 (f) of 770 K case) at 0.104 ms. And a significant super-knock with pressure oscillation  $\Delta P_{max} = 10.0$  MPa ( $KI = 5$ ), was captured. For the case of  $T_{eoc} = 770$  K, a strong pressure pulse, 10.0 MPa, indicates the super-knock and two bright hot-spots may be related to the transition to detonation. Wang et al. [22] observed a similar strong pressure oscillation and hot-spot induced detonation when investigate the auto-ignition process of *i*-octane under  $T_{eoc} = 930$  K and  $P_{eoc} = 2.0$  MPa.

To investigate the impact of equivalence ratios on the ignition modes of naphtha/oxygen mixtures, the monochrome images for four different  $\phi = 0.8, 1.0, 1.2$  and  $1.5$  at  $T_{eoc} = 710$  K,  $P_{eoc} = 2.0$  MPa, were presented together with the BMF and pressure traces in Fig. 9. However, the monochrome images at a lean  $\phi = 0.5$  display very low luminance, which is attributed to the relatively low combustion temperatures, posing challenges for their capture with the current high-speed camera. All four cases have the onset of auto-ignition spot initiated at the left top side of cylinder, which propagated into the center of combustion chamber in a similar direction. Under these conditions, end-gas auto-ignition did not occur, probably because, prior to the trigger of end-gas auto-ignition, all unburned mixtures had already combusted through the reaction wave.

The time history of BMF and pressure evolution in Fig. 9 indicates that the mixtures at  $\phi = 1$  and  $1.2$  conditions burned slightly faster than those at  $\phi = 0.8$  and  $1.5$ , though the difference is not marked. Almost identical BMF evolution is observed for  $\phi = 1$  and  $1.2$ . This observation is consistent with previous measurements [29] that the laminar burning velocity has a parabolic relationship with equivalence ratio, peaking around  $\phi = 1.1$ , and shows nearly identical laminar burning velocities at  $\phi = 1$  and  $\phi = 1.2$ , may explain the similar BMF trends observed. The pressure curves for all mixtures are smooth and knock-free, with the  $\phi =$

$1.2$  and  $1.5$  mixtures showing the highest peak pressure at 7.5 MPa. In contrast, the lean mixture with  $\phi = 0.5$  exhibits the lowest peak pressure of 4.5 MPa and takes almost 4 ms to reach this peak, compared to just 1.5 ms for the other mixtures.

The impact of pressure,  $P_{eoc}$ , on the ignition mode of naphtha is depicted in Fig. 10. Three different pressures, 1.0 MPa, 1.5 MPa and 2.0 MPa, were obtained by adjusting the mole fraction of diluent in the stoichiometric naphtha/oxygen mixture at  $T_{eoc} = 710$  K. The onset auto-ignition of all three cases were initiated at the top-left of cylinder, and then propagated towards the center of combustion chamber. The plot of BMF shows the coal-based naphtha burnt much slower at the elevated pressure. Overall, under the current measurements, it has been observed that the ignition of coal-based naphtha did not exhibit purely homogeneous behavior that may be caused by the inhomogeneity of temperature field, as it consistently localized near the cylinder wall.

### 3.4. Visualization of knock initiation

The pressure trace and monochrome images showing the reaction wave propagation for a normal knock case of lean  $\phi = 0.8$  naphtha/oxygen mixture at  $T_{eoc} = 770$  K and  $P_{eoc} = 2.0$  MPa are presented in Fig. 11. The pressure value corresponding to each image is labelled using alphabetic letter to track the pressure fluctuation at the onset of knock. The onset of auto-ignition was initiated at the top-left region of cylinder and propagated into the center of cylinder. The pressure trace rose gradually at first, then started to fluctuate from 0.282 ms after the auto-ignition. The end-gas auto-ignition (bright region labelled as knock initiation in Fig. 11 (f)) was triggered at the bottom of cylinder before the reaction wave front approaching.

The pressure trace and the monochrome images showing the super-knock development of stoichiometric naphtha/oxygen mixture at  $P_{eoc} = 2.0$  MPa,  $T_{eoc} = 770$  K, are presented in Fig. 12. The onset of auto-ignition is located on the top left of image and propagating into the center of cylinder. At 0.045 ms after the onset of auto-ignition, a bright spot is formed on the top of cylinder indicating the initial of knock followed by a strong pressure oscillation,  $\Delta P_{max} = 10$  MPa, on the pressure trace. After that at 0.09 ms, another detonation-like ignition spot was initiated at the bottom of image indicating the onset of super-knock. Thereafter, the significant pressure oscillation is related to the reflection of reaction wave within the cylinder wall. The formation of detonation pulse in Fig. 12 (g) is a typical end-gas auto-ignition since the compression effect by the propagating reaction wave increases the temperature and pressure of the unburned mixtures at the bottom of cylinder, which favors the strong auto-ignition [24].

### 3.5. Knock map

To better illustrate the regimes of ignition mode, a knock map (see Fig. 13) has been constructed for coal-based naphtha based on the value of  $KI$  derived from pressure traces in current measurements. The knock-free regime sits at low temperature  $T_{eoc} = 640$  K, 670 K, 690 K and 710 K, encompassing all equivalence ratios. At  $T_{eoc} = 740$  K, the behavior varies with  $\phi = 0.5$  and  $0.8$  are knock free, while  $\phi = 1, 1.2, 1.5$  experience normal knock. Super-knock begins at  $T_{eoc} = 770$  K with  $\phi = 1$ . However, when the  $T_{eoc}$  increases to 830 K, the knock boundary shifts from  $\phi = 0.8$  to the leaner side  $\phi = 0.5$ . At 900 K, the super-knock dominates the ignition mode, even at  $\phi = 0.5$ . Overall, the  $T_{eoc}$  primarily dominates the modes of knock, with both knock and super-knock occurring under high  $T_{eoc}$  conditions. Lean mixtures, characterized by low  $\phi$  values, are less prone to knocking. However, as the mixture becomes richer, the tendency to knock increases, indicating that knock behavior is not solely dependent on the  $T_{eoc}$ .

### 3.6. Detonation peninsula, $\xi$ - $\varepsilon$ diagram

Although the knock map is useful for qualitatively identifying the

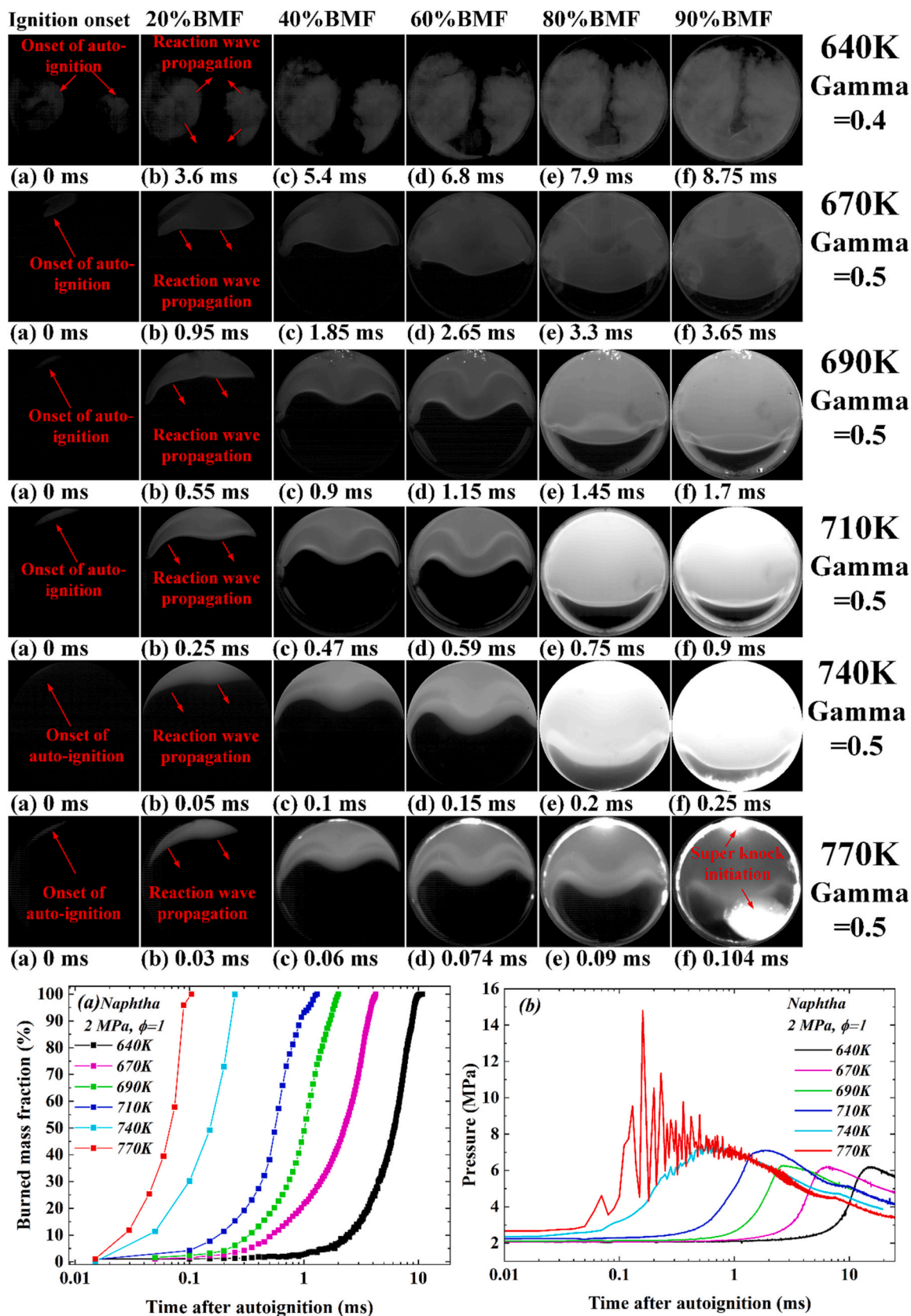


Fig. 8. Monochrome image sequences, burned mass fraction and pressure trace for stoichiometric coal-based naphtha/oxygen mixtures at  $T_{eoc} = 640, 670, 690, 710, 740$  and  $770$  K and  $P_{eoc} = 2.0$  MPa.

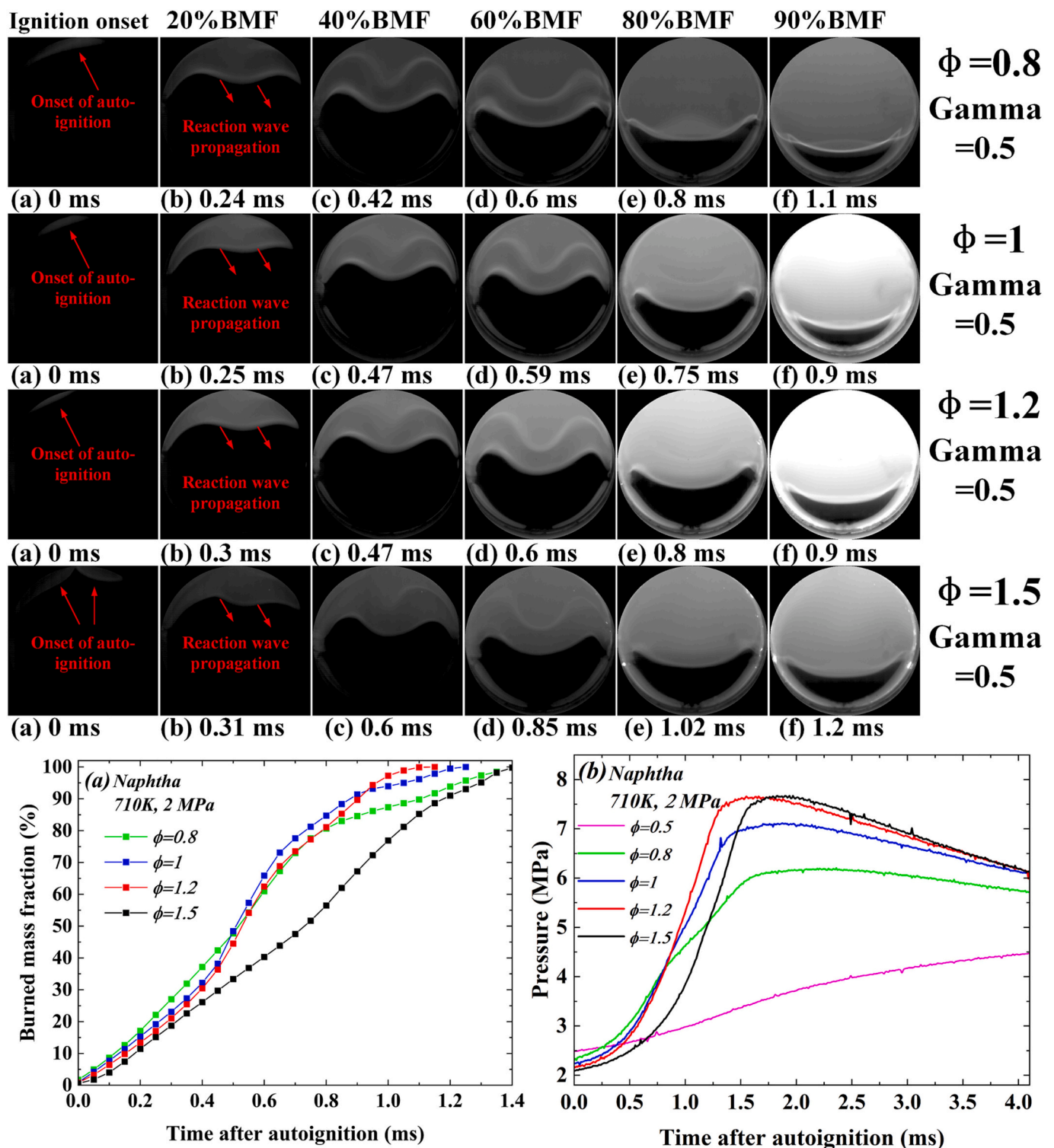


Fig. 9. Monochrome image sequences, burned mass fraction and pressure trace for coal-based naphtha/oxygen mixtures at various  $\phi = 0.8, 1, 1.2,$  and  $1.5$  under  $T_{eoc} = 710$  K and  $P_{eoc} = 2.0$  MPa.

regimes of knock, it is essential to develop dimensionless groups to quantitatively elucidate the ignition modes of coal-based naphtha. The dimensionless  $\xi$ - $\epsilon$  diagram has been widely employed to empirically study the knocks in engines conditions. Kalghatgi et al. [27] implemented this approach to study the nature of knock and identify the super-knock regime in engines. Robert et al. [50] employed a hybrid large eddy simulation and the  $\xi$ - $\epsilon$  diagram to predict the DDT in a downsized spark ignition engine. More recently, Gorbatenko et al. [39]

combined the chemical kinetics and  $\xi$ - $\epsilon$  diagram to study the auto-ignitive and anti-knock properties of *n*-butanol. Moreover, the  $\xi$ - $\epsilon$  diagram was employed to study the NTC effect and DDT of *i*-octane in an optical RCM [25]. The dimensionless parameter  $\xi$  is relevant to the development of detonation, defined as the ratio of local acoustic velocity over auto-ignitive velocity:

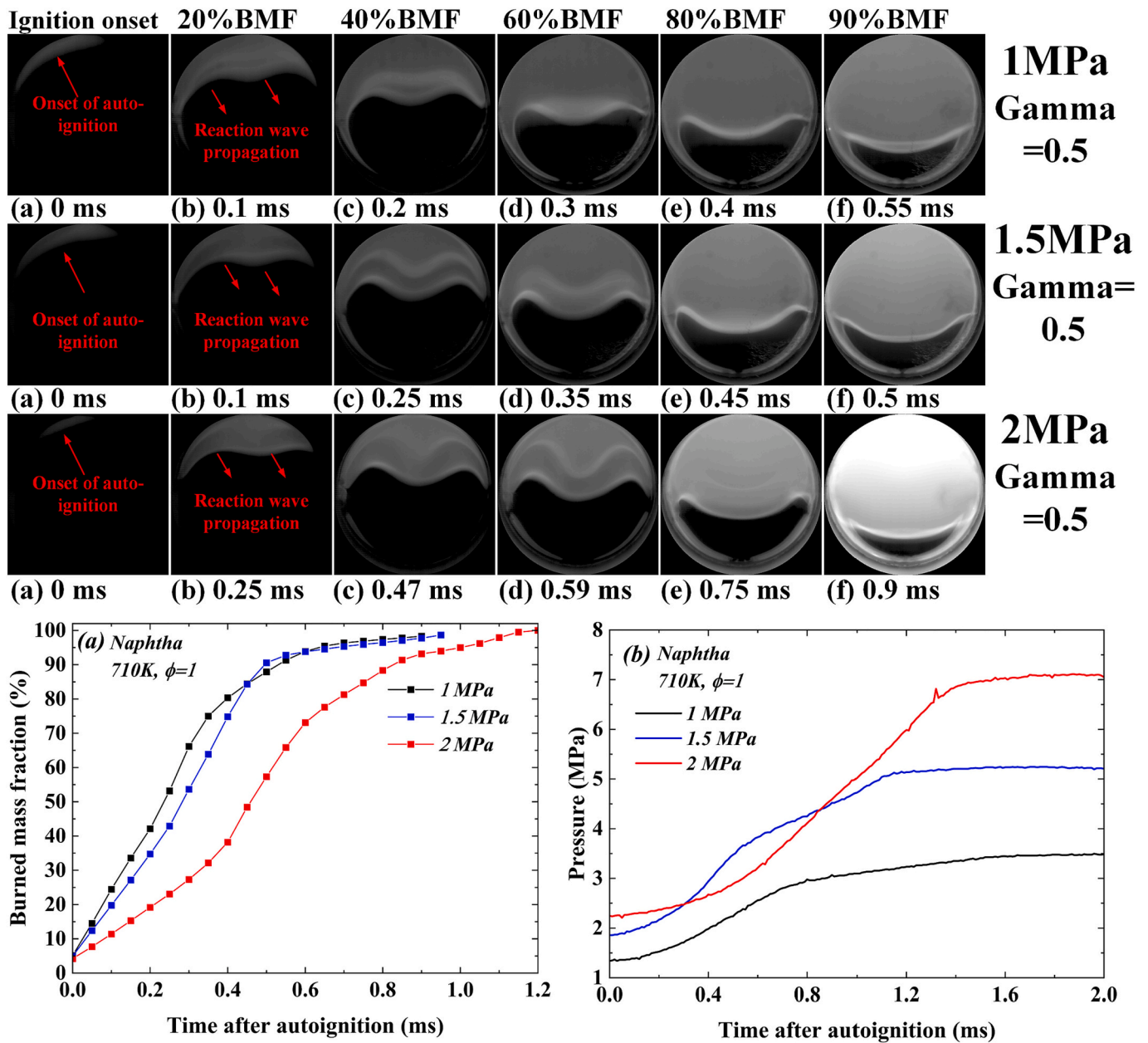


Fig. 10. Monochrome image sequences, burned mass fraction and pressure trace for stoichiometric coal-based naphtha/oxygen mixtures at various  $P_{eoc} = 1.0, 1.5$  and  $2.0$  MPa under  $T_{eoc} = 710$  K.

$$\xi = \frac{a}{u_a} = a \left( \frac{\partial T}{\partial r} \right) \left( \frac{\partial \tau_i}{\partial T} \right) \quad (2)$$

where,  $a$  is the acoustic velocity through the reactive mixture,  $u_a$  is the auto-ignitive velocity. The unity value of  $\xi$  indicates the reaction wave coupling with the acoustic wave representing the transition to detonation. The acoustic velocity  $a$  depending on temperature, pressure, and mixture strength, were calculated using the GASEQ code [51]. The auto-ignitive velocity is defined as:

$$u_a = \frac{\partial r}{\partial \tau_i} = \left( \frac{\partial r}{\partial T} \right) \left( \frac{\partial T}{\partial \tau_i} \right). \quad (3)$$

This theoretical auto-ignitive speed is derived from the Zeldovich hot spot temperature gradient theory [36] and the temperature gradient inside the hot spot,  $\frac{\partial T}{\partial r}$ , and the temperature gradient with respect to the  $\tau_i$ ,  $\frac{\partial \tau_i}{\partial T}$ , need to be determined. The gradient  $\frac{\partial T}{\partial r}$  is established from the DNS

study [17], which simulated a detonation developing rapidly from a hot spot in a stoichiometric mixture of  $H_2$ -CO-air, revealing a value around  $-2$  K/mm. Following the work on hydrocarbons (*i*-octane, *n*-heptane and *n*-butanol and toluene reference fuel) in [25,27,28,39] the assumption of  $\frac{\partial T}{\partial r} = -2$  K/mm is adopted for naphtha in this study.

To determine  $\frac{\partial \tau_i}{\partial T}$  a correlation of  $\tau_i$  and  $\tau_e$  as a function of  $T$  and  $P$  proposed by Kalghatgi et al. [27] is adopted here:

$$\tau_i, \tau_e = A \times e^{(B/T)} \times \left( \frac{P}{2} \right)^C \quad (4)$$

For the NTC regime (770–880 K)

$$\tau_i = A \times e^{(B \times T)} \times \left( \frac{P}{2} \right)^C \quad (5)$$

By matching the predicted  $\tau_i$  and  $\tau_e$  in Figs. 14 and 15, the constants A, B and C in the correlation can be derived via a multiple-regression

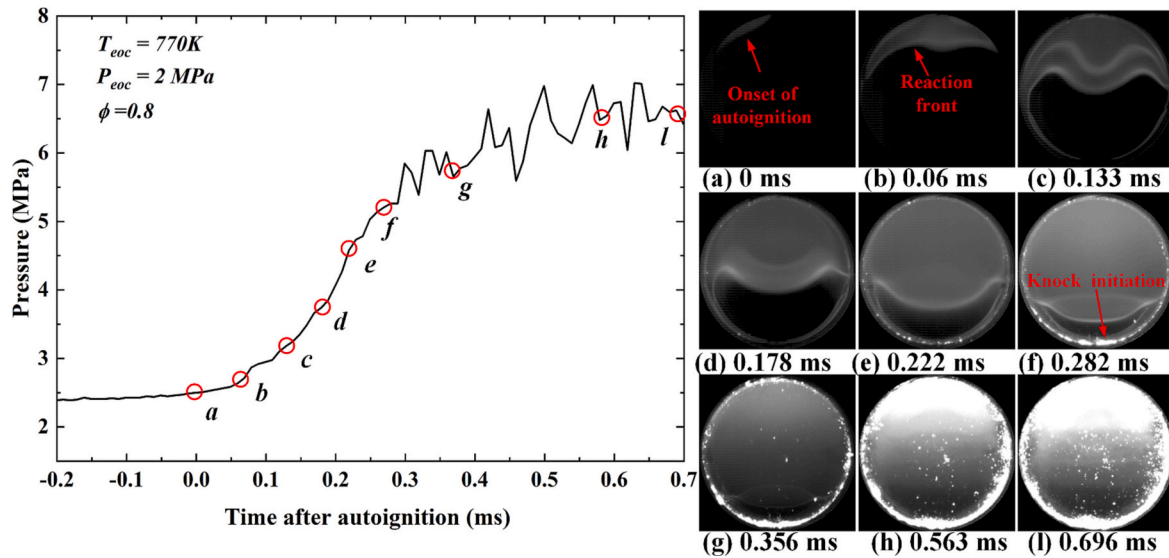


Fig. 11. Pressure trace and monochrome image sequences for the knock case of coal-based naphtha under  $T_{eoc} = 770$  K,  $P_{eoc} = 2.0$  MPa,  $\phi = 0.8$ .

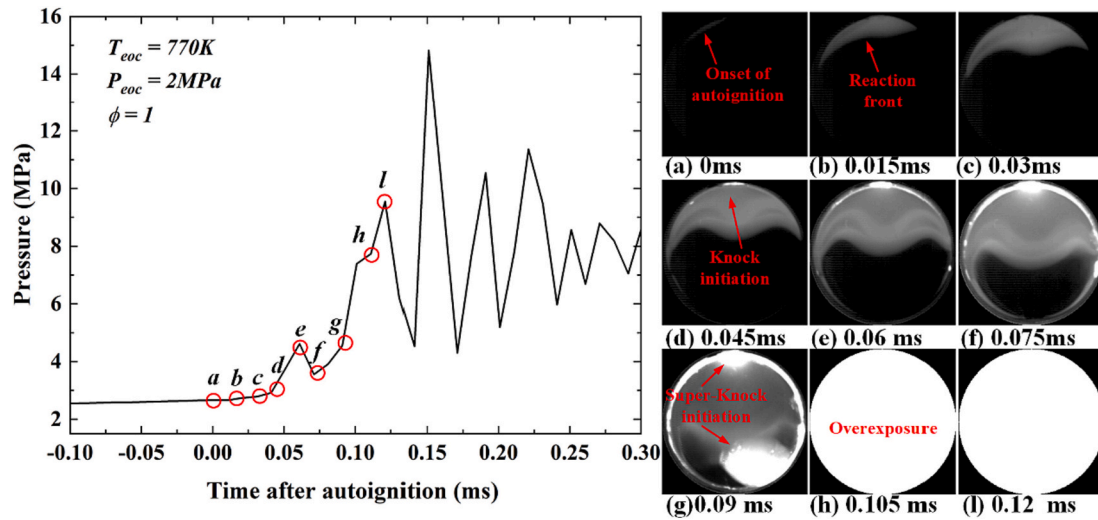


Fig. 12. Pressure trace and monochrome image sequences of coal-based naphtha at  $T_{eoc} = 770$  K,  $P_{eoc} = 2.0$  MPa and  $\phi = 1.0$ . Image (a) showing the onset of auto-ignition, (b) for the reaction front, (d) for the onset of knock, (g) for the super-knock initiation.

method, see Table 4. To thoroughly investigate the transition of end-gas ignition modes during the reaction wave propagation in RCM, it is necessary to examine the effects of temperature and pressure on  $\tau_i$  and  $\tau_e$ , extending up to 1250 K and 10 MPa, respectively, as shown in Figs. 14 and 15. This approach allows gaining an insight on the variation of  $\tau_i$  and  $\tau_e$  during the reaction wave propagation in which the in-cylinder pressure and temperature present dynamic change.

The partial derivative of Eqs. (4) & (5) with respect to temperature yields Eqs. (6) & (7), respectively:

$$\partial\tau_i/\partial T = B \times \tau_i/T^2 \quad (6)$$

For the NTC regime (770–880 K)

$$\partial\tau_i/\partial T = B \times \tau_i \quad (7)$$

The  $\tau_i$  of naphtha/air mixture is predicted using the 3-component surrogate model with LLNL mechanism as afore-discussed in Section 3.2. Although the predictions from this mechanism do not align with the measured  $\tau_i$  at temperatures beyond 770 K at 2 MPa, they still retain value for empirical analysis in delineating ignition modes through the  $\xi$ - $\epsilon$  diagram.

Another dimensionless parameter  $\epsilon$  indicates the energy fed rate from a reactive hot spot with radius  $r_0$ , into an auto-ignitive flow, written as:

$$\epsilon = \frac{r_0}{a\tau_e} \quad (8)$$

where  $r_0$  is the hot spot radius and  $\tau_e$  is the chemical excitation time. The ratio of  $r_0$  over  $a$  indicates the residence time of acoustic wave inside the hot spot. The present study adopts a 5 mm hot spot radius, which corresponds to the turbulent flow length scales and heterogeneities in SI engines. The selection of this radius remains consistent with the assumption made in previous works [25,27,28,39]. The excitation time,  $\tau_e$  presents the period of rapid thermal energy release, and is defined as the duration from 5% of maximum heat release rate to its maximum value during the auto-ignition process [52]. The predicted  $\tau_e$  as a function of temperature and pressure are presented in Fig. 15 for stoichiometric coal-based naphtha/air mixture. A similar correlation (Eq. (4) with constants in Table. 4) for  $\tau_e$  has been derived by fitting the predicted data, and then implemented in Eq. (8) to calculate  $\epsilon$ .

As shown in Fig. 12 (g), the end-gas autoignition occurs when the

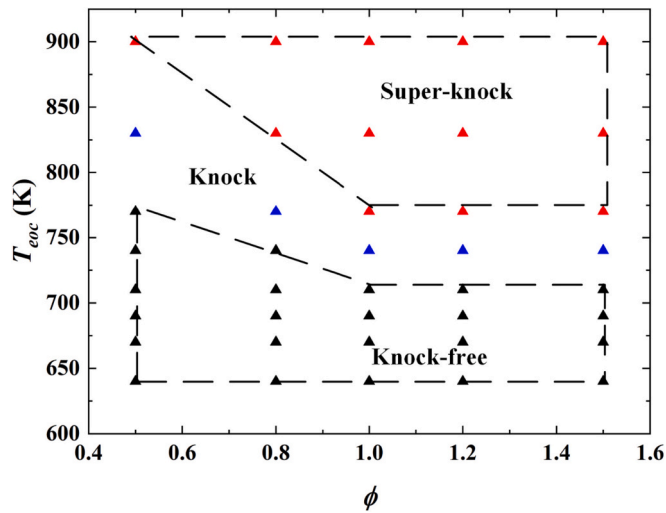


Fig. 13. Knock map of coal-based naphtha/oxygen based on end of compression temperature and equivalence ratio.

propagating reaction wave compresses the unburned mixture to the auto-ignition temperature,  $T_{ai}$  and the auto-ignition pressure,  $P_{ai}$ , leading to the super-knock which is possibly related to the transition to detonation. Neglecting the heat loss during the compression of reaction wave,  $T_{ai}$  can be determined by the isentropic compression law of Eq. (9):

$$T_{ai} = T_{eoc} \left( \frac{P_{ai}}{P_{eoc}} \right)^{\frac{\gamma-1}{\gamma}}, \quad (9)$$

$P_{ai}$  is taken from the pressure trace. Both  $T_{ai}$  and  $P_{ai}$  were the key inputs for calculating  $\tau_i$  and  $\tau_e$  (Eqs. (4) and (5)), which were then used to determine the dimensionless parameters  $\xi$  and  $\varepsilon$ . The value of  $\xi$  and  $\varepsilon$  were located on the detonation peninsula for identifying the

corresponding ignition modes. For each explosion, four instantaneous points along the pressure trace from the first observed onset of auto-ignition to the peak value are selected with uniform pressure increment. These pressure points,  $P_{ai}$  provide the crucial inputs in Eq. (9), for observing full history of ignition modes during reaction proceeding. The auto-ignition parameters for  $\xi$ - $\varepsilon$  diagram and the corresponding ignition modes of stoichiometric coal-based naphtha under  $P_{eoc} = 2$  MPa and  $T_{eoc} \in 640$ – $900$  K are listed in Table 5.

The evolution of ignition mode (consisting of 4 consecutive time transients during the auto-ignition) of naphtha/oxygen mixture within RCM under  $T_{eoc} = 640$  K and  $710$  K are super-imposed on the  $\xi$ - $\varepsilon$  detonation peninsula diagram in Fig. 16, where  $\xi_u$  and  $\xi_l$  indicate the upper boundary and lower boundary for the transition to detonation, respectively. The value of  $\xi_u$  and  $\xi_l$  are taken from engine experiments and modelling in [18,28,29]. Triangle symbols are corresponding to different time transients during the single explosion and the instant pressure,  $P_{ais}$ , taken from the pressure trace sits nearby the symbol. In general, the combustion events in both cases commenced in the regime of subsonic auto-ignition and eventually ended in the same regime. As the combustion evolving in the RCM,  $P_{ai}$  and  $T_{ai}$  rose up, which favors a faster auto-ignitive velocity,  $u_a$ , (shown in Eq. (3)) and a shorter excitation time,  $\tau_e$ , (depicted in Eq. (4)). Consequently, this led to a smaller value of  $\xi$  and a higher value of  $\varepsilon$ .

However, under a higher  $T_{eoc} = 710$  K, the end of combustion is closer to the developing detonation peninsula because of higher  $T_{ai} = 883$  K and  $P_{ai} = 6.2$  MPa. Recalling the pressure traces and reaction wave propagation images in Fig. 8 for both cases, no pressure pulse and end-gas auto-ignition were observed, which serves as convincing evidence supporting the conclusion on subsonic auto-ignitive propagation in  $\xi$ - $\varepsilon$  diagram.

The evolution of auto-ignition event of stoichiometric coal-based naphtha mixtures at intermediate temperatures (770 K, 830 K and 900 K) in RCM are presented in Fig. 17. Starting with the case of  $T_{eoc} = 770$  K, it started at subsonic auto-ignition regime and ended in the regime of developing detonation with  $P_{ai} = 7.5$  MPa and  $T_{ai} = 1035$  K

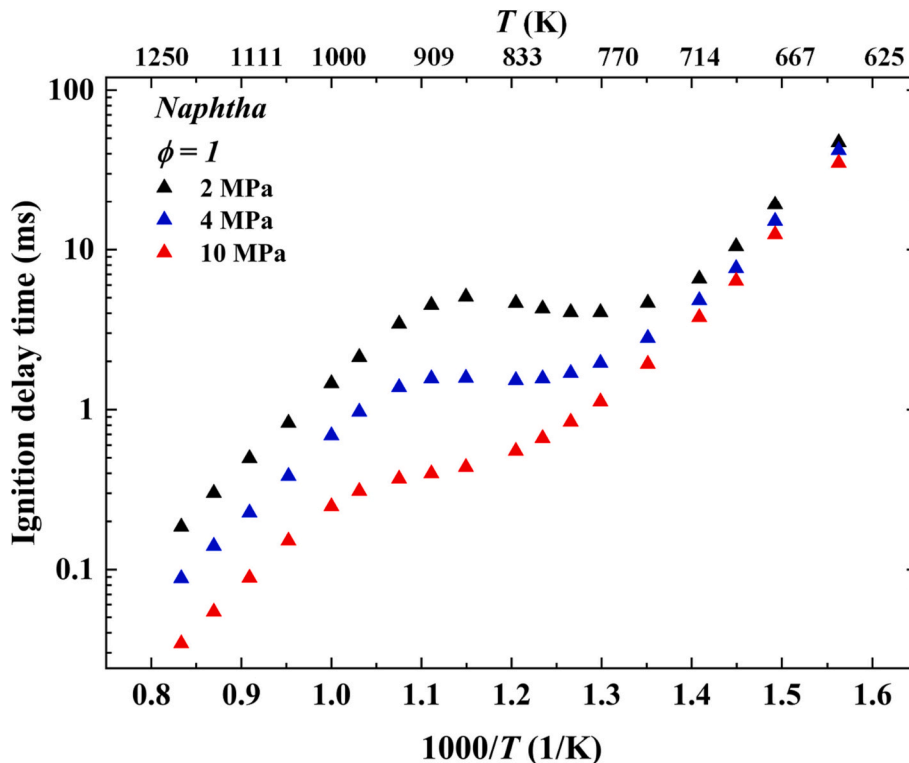


Fig. 14. Modeled  $\tau_i$  of stoichiometric coal-based naphtha/air mixture at 2.0, 4.0 and 10.0 MPa by using the 3-component surrogate model.

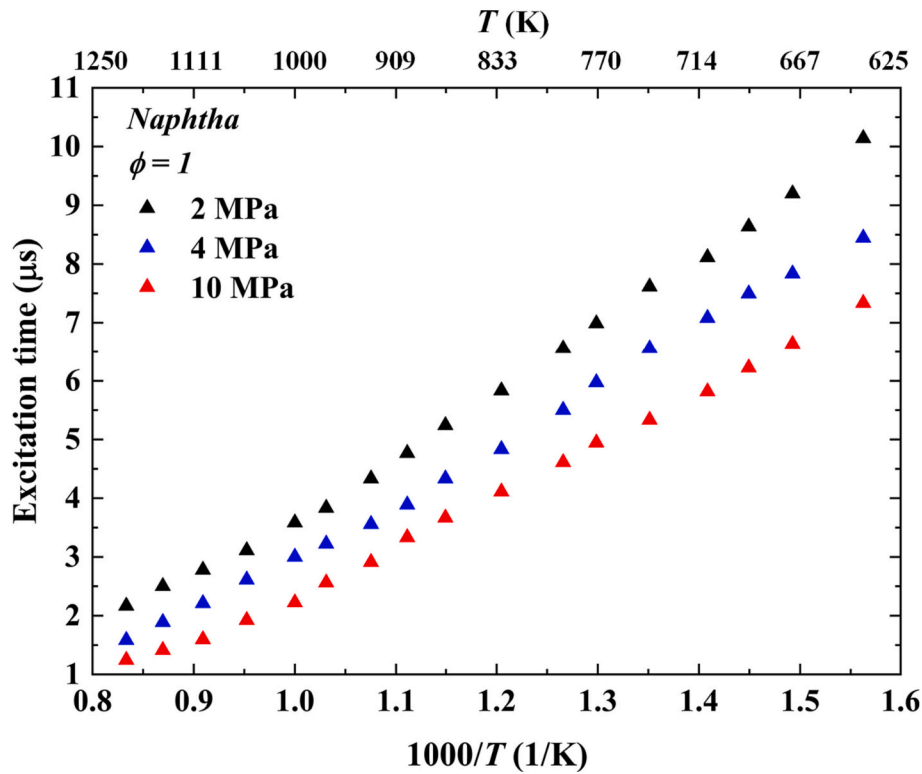


Fig. 15. Predicted excitation time of stoichiometric coal-based naphtha/air by 3-component surrogate model.

Table 4  
Constants A, B and C for  $\tau_i$  and  $\tau_e$  in coal-based naphtha.

Temperature	$\tau_i$			$\tau_e$	
	640–770 K	770–880 K	880–1200 K	640–970 K	970–1200 K
A	$4.04 \times 10^{-6}$	0.25	$3.92 \times 10^{-6}$	0.5	0.17
B	10,253	0.0035	12,803	2000	3023
C	-0.4	-1.5	-1	-0.23	-0.3

Table 5  
Auto-ignition parameters of stoichiometric coal-based naphtha mixtures at auto-ignition pressure,  $P_{ai}$ , and auto-ignition temperature,  $T_{ai}$ .

$P_{eoc}$ (MPa)	$T_{eoc}$ (K)	$P_{ai}$ (MPa)	$T_{ai}$ (K)	$a$ (m/s)	$\tau_e$ ( $\mu$ s)	$\tau_i$ (ms)	$u_a$ (m/s)	$\epsilon$	$\xi$	Ignition mode
2.0	640	2.1	644	406	11	32.5	0.62	1.12	653	Subsonic auto-ignition
2.0	640	3.4	701	423	7.7	7.35	3.3	1.54	130	Subsonic auto-ignition
2.0	640	4.5	734	431	6.3	3.4	7.7	1.83	55.8	Subsonic auto-ignition
2.0	640	5.8	769	444	5.3	1.63	17.7	2.14	25.1	Subsonic auto-ignition
2.0	710	2.2	724	462	7.7	5.5	4.7	1.4	99.4	Subsonic auto-ignition
2.0	710	3.5	769	472	5.9	2	14.5	1.8	32.6	Subsonic auto-ignition
2.0	710	5	844	501	4.3	1.21	54.5	2.3	9.2	Subsonic auto-ignition
2.0	710	6.2	883	510	3.8	1.07	70.8	2.58	7.2	Subsonic auto-ignition
2.0	770	2.5	784	527	6.4	3.44	41	1.47	12.5	Subsonic auto-ignition
2.0	770	3.3	861	541	4.4	2.4	59.5	2.1	9.1	Subsonic auto-ignition
2.0	770	6.0	984	567	3.3	0.58	85	2.7	6.7	Subsonic auto-ignition
2.0	770	7.5	1035	596	2.4	0.25	170	3.5	3.5	Developing detonation
2.0	830	2.1	839	524	5.0	4.4	17.5	1.9	30	Subsonic auto-ignition
2.0	830	4.2	992	563	3.1	0.75	51	2.9	11	Subsonic auto-ignition
2.0	830	5.6	1054	601	2.2	0.26	164	3.7	3.7	Developing detonation
2.0	830	7.0	1101	613	1.9	0.13	376	4.4	1.6	Thermal explosion
2.0	900	2.1	911	528	4.1	4.7	6.8	2.3	77	Subsonic auto-ignition
2.0	900	3.5	1034	599	2.3	0.53	78	3.6	7.7	Subsonic auto-ignition
2.0	900	4.4	1088	604	1.9	0.24	196	4.3	3.1	Developing detonation
2.0	900	6.0	1181	630	1.4	0.08	700	5.5	0.9	Thermal explosion

indicating a successful transition to detonation. As discussed in section 3.3, the end-gas ignition for 770 K was followed by a super-knock pressure oscillation, and the combustion luminosity images showed the bright detonation-like spot initiated the onset of super-knock. The  $\xi$ - $\epsilon$  detonation peninsula diagram suggests the end-gas ignition mode of 770 K is a detonation. For both 830 K and 900 K, the auto-ignitions started with the subsonic auto-ignition regime. As the combustion proceeded, rising  $P_{ai}$  crossed the regime of developing detonation and eventually ended up in the thermal explosion regime, where the instantaneous homogeneity explosion dominated the ignition mode.

Although no optical measurement for higher temperature conditions (> 770 K) due to safety consideration, the localized pressure traces (see Fig. 21) demonstrate an instantaneous pressure rise to peak value

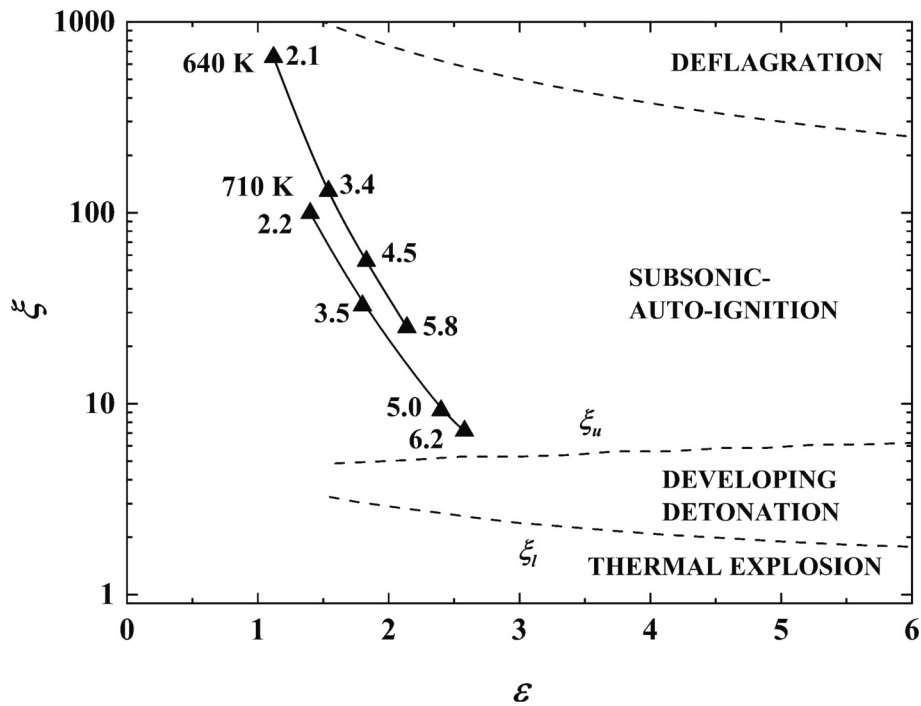


Fig. 16.  $\xi$ - $\varepsilon$  diagram for stoichiometric coal-based naphtha mixtures with  $T_{eoc} = 640$  K and  $710$  K in this study, the boundary of  $\xi_u$  and  $\xi_l$  from the engine experiments and modelling in [18,28,29]. The representative values of instant  $P_{ai}$  through the ignition process lie next to the symbols.

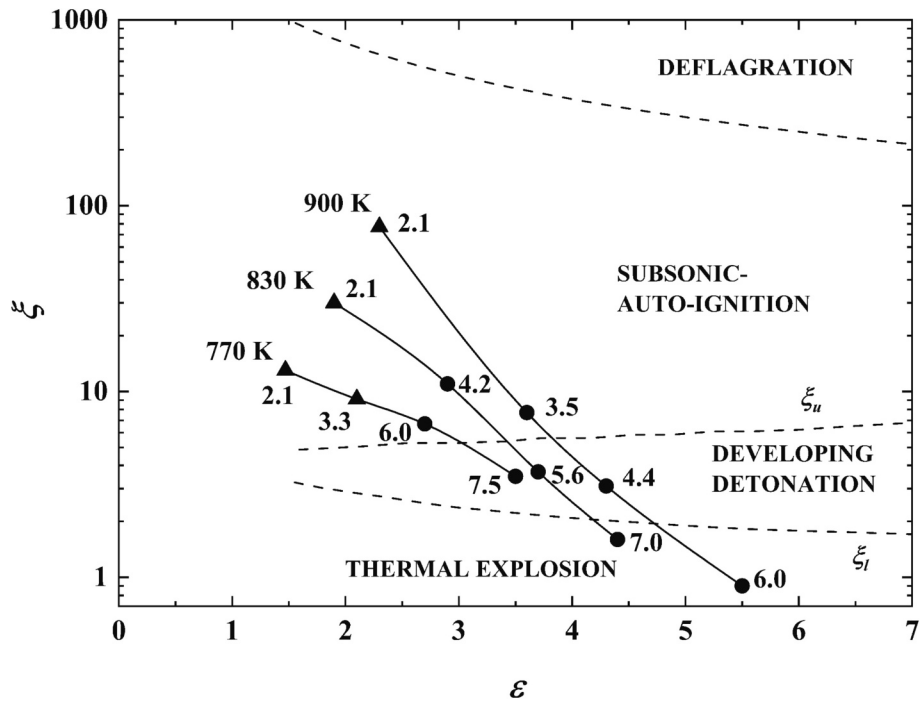


Fig. 17.  $\xi$  -  $\varepsilon$  diagram for stoichiometric coal-based naphtha mixtures at different  $T_{eoc} = 770$  K,  $830$  K and  $900$  K in this study. The value  $T$  nearby the symbols presenting the  $P_{ai}$  in MPa.

(within 0.2 ms) occurred in the case of  $T_{eoc} = 830$  K and  $900$  K. Such an instantaneous pressure rise followed with strong oscillation must correspond to the event of thermal explosion as depicted in Fig. 18.

### 3.7. Heat release rate analysis

Previous studies [24,28,53] reported that the amplitude of the

pressure pulse generated at the hot spot is governed by the magnitude of maximum Heat Release Rate (HRR). When this HRR is sufficiently high, it can cause the pressure pulse to couple with a detonation wave, indicating a transition to detonation. The progression from auto-ignition to detonation, and ultimately to thermal explosion, is closely tied to the variations in the maximum HRR under different initial conditions of temperature and pressure. To further understand this relationship, the

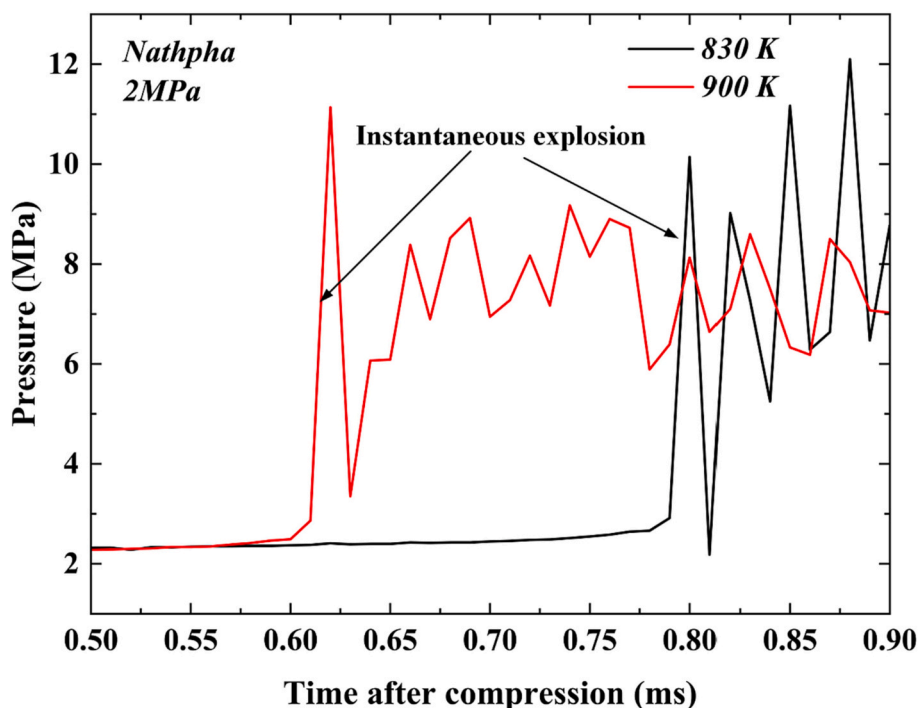


Fig. 18. Localized pressure traces for stoichiometric coal-based naphtha/air mixture at  $T_{eoc} = 830$  K, 900 K and  $P_{eoc} = 2$  MPa.

maximum volumetric HRRs were exported when performing the IDTs calculation for coal-based naphtha using the CHEMKIN-PRO software [33] with a 3-component surrogate model under closed homogeneous batch reactor conditions. The maximum volumetric HRRs for five different  $P_{ai}$  and corresponding  $T_{ai}$  sets covering the ignition modes from auto-ignition to detonation and thermal explosion are depicted in Fig. 19.

The temperature ranges from 778 K to 1035 K provided the full history of heat release rate during the reaction proceeding of  $T_{eoc} = 770$  K. It is observed that within the temperature range of 778 K to 984 K, the ignition mode was auto-ignition, in which maximum HRR increased from 1400 to 12,000 kW/cm<sup>3</sup> as the chemical reaction proceeds. The increase in HRR reflects the increasing strength of auto-ignition.

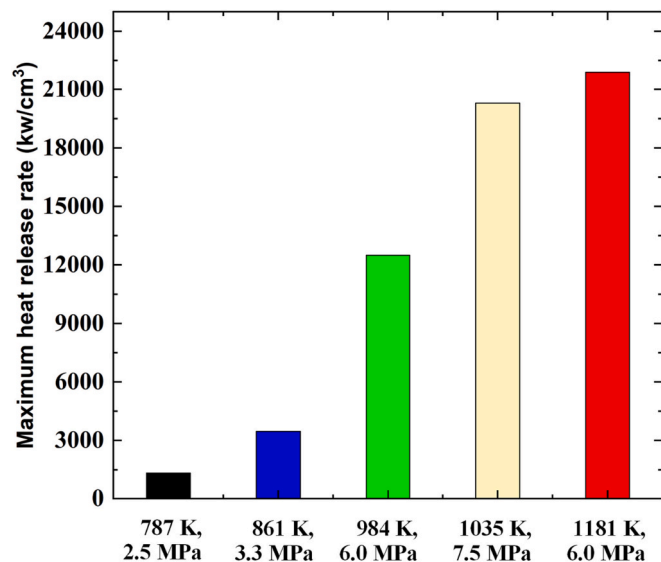


Fig. 19. Maximum HRRs during the auto-ignition of stoichiometric coal-based naphtha/air mixture at conditions covering the full ignition modes from subsonic auto-ignition to thermal explosion.

Eventually, a transition to detonation occurred under the condition of  $T_{ai} = 1035$  K and  $P_{ai} = 7.5$  MPa corresponding to the maximum HRR of 20,000 kW/cm<sup>3</sup>. Furthermore, under the condition of  $T_{ai} = 1181$  K and  $P_{ai} = 6.0$  MPa a thermal explosion of  $T_{eoc} = 930$  K required the maximum heat release rate of 22,000 kW/cm<sup>3</sup>.

To deepen the foundational understanding of the HRR, the normalized HRRs (i.e. the ratio of the maximum HRR of each reaction to the summed maximum HRR) with respect to the top six reactions determined via sensitivity analysis are shown in Fig. 20 for stoichiometric coal-based naphtha/air mixture. The exothermic reactions have positive normalized HRRs, while negative values for endothermic reactions. The chain-branching reaction  $H_2O + M < \geq H + OH + M$  dominates the HRR under all conditions, accounting for 30% of the total. This finding is consistent with [54] that claimed the knock of hydrocarbons may be connected with a competition between the chain-branching reactions  $H_2O + M < \geq H + OH + M$  and  $H + O_2 < \geq O + OH$ . For the radical-recombination reaction  $HCCO + OH < \geq H_2 + CO + CO$ , it tends to be strengthened as temperature and pressure increase. The chemiluminescence spectroscopy and chemical-kinetic analysis within an HCCI engine [55] also suggested that the high-temperature heat-release of *i*-octane and PRF80 fuels be primarily governed by the formation of CO radical. In contrast, the occurrence of the reaction  $CO + OH < \geq CO_2 + H$  diminishes with increasing temperature and pressure. In general, the occurrence of detonation is associated with high values of heat release rate. At the scale of chemical kinetics, the chain-branching reaction  $H_2O + M < \geq H + OH + M$  dominates the heat release in all ignition modes, including auto-ignition, detonation, and thermal explosion. Additionally, an increase in the heat release rate from the radical-recombination reaction  $HCCO + OH < \geq H_2 + CO + CO$  promotes the transition towards detonation and even thermal explosion.

#### 4. Conclusions

In the current study, the IDTs of coal-based naphtha/oxygen mixtures was measured with a wide range of temperatures, equivalence ratio and pressure within Leeds optical RCM. IDTs of coal-based naphtha/oxygen decreases with the increasing of temperature,

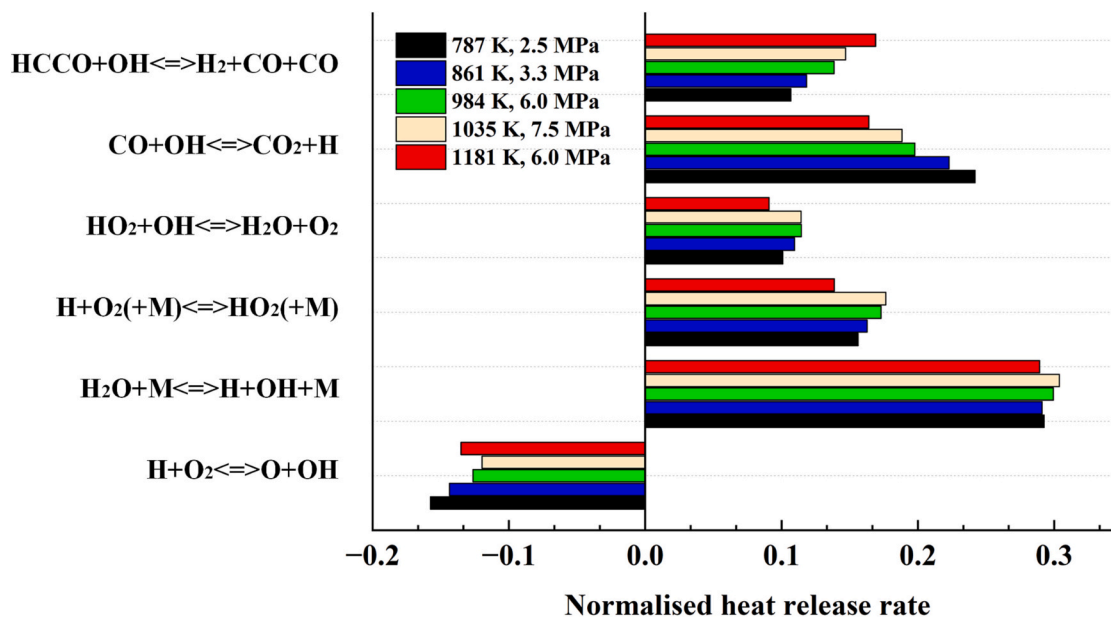


Fig. 20. Normalized HRRs of top six chemical reactions for stoichiometric coal-based naphtha/air mixture at different ignition modes: auto-ignition, detonation and thermal explosion.

pressure and equivalence ratio. The apparent NTC behavior was observed at  $P_{eoc} = 1.0$  MPa, 1.5 MPa, and it shifted to the higher temperature regime as the pressure increased. Moreover, the IDTs of stoichiometric naphtha are between that of *i*-octane and *n*-heptane as expected as a low octane number fuel. The 3-components naphtha surrogate models based on the LLNL and FACE kinetics were employed to predict the IDTs, excitation time and HRR of coal-based naphtha under closed homogeneous batch reactor conditions using the CHEMKIN-PRO software. Compared with measured data, the kinetics fitted well at the low temperature range 640–740 K, but overpredicted at the temperature range of 770–900 K.

The natural combustion luminosity images were captured and then were used to derive the fuel BMF during the overall ignition period of naphtha. The BMF plots show that the temperature dominates the burning speed and the fuel burning faster within stoichiometric or slightly rich conditions while slower in the lean and rich conditions, but the burning speed decreasing with the increasing of pressure. The initial ignition of coal-based naphtha did not exhibit purely homogeneous behavior, as it consistently localized near the cylinder wall. The combination of images and pressure traces illustrated that the onsets of knock and super-knock were related to the initiation of detonation-like hot spots before the arrival of the primary reaction wave. The knock map presents both temperature and equivalence ratio have effects on the ignition modes. The knock and super-knock trends to occur at high temperatures and rich equivalence ratio regimes.

The Bradley's  $\xi$ - $\epsilon$  diagram was employed to assess the ignition modes of coal-based naphtha. For 640 K and 710 K cases, the whole ignition process sits on the subsonic auto-ignition regime. As  $T_{eoc}$  raising to 770 K, the ignition modes started with subsonic auto-ignition and finally ended in the developing detonation regime representing the transition to detonation. The super-knock pressure oscillation, detonation pulse images and  $\xi$ - $\epsilon$  parameters all provided the evidence that the super-knock was related to the transition of detonation. The high heat release rates often coincided with detonation occurrences, with the chain-branching reaction  $\text{H}_2\text{O} + \text{M} \rightleftharpoons \text{H} + \text{OH} + \text{M}$  predominantly contributing to heat release across all ignition modes.

#### CRedit authorship contribution statement

Jinzhou Li: Writing – original draft, Visualization, Methodology,

Investigation, Formal analysis. An Lu: Writing – review & editing, Validation, Resources, Formal analysis. Yu Xie: Writing – review & editing, Validation, Investigation, Formal analysis, Data curation. Junfeng Yang: Writing – review & editing, Supervision, Resources, Funding acquisition, Conceptualization. Chunhua Zhang: Writing – review & editing, Supervision, Resources.

#### Declaration of competing interest

The authors declare that they have no known competing financial interests or personal relationships that could have appeared to influence the work reported in this paper.

#### Data availability

Data will be made available on request.

#### Acknowledgements

The authors wish to thank Professor Derek Bradley for the insightful discussions, which greatly contributed to this research. Mr. An Lu would like to express sincere thanks to the China Scholarship Council for their generous financial support (Grant No. CSC202106567003) during his academic visit to the University of Leeds. Yu Xie acknowledges the China Scholarship Council and the University of Leeds for a joint PhD scholarship (Grant No. CSC202008350141). The authors extend their gratitude to UFA-Tech Co., Ltd. (Shanghai) for conducting the MON value test and providing insightful discussions.

#### References

- [1] International Energy Agency. CO2 emissions in 2022. 2022.
- [2] Park W. Naphtha as a fuel for internal combustion engines. *Int J Automot Technol* 2021;22:1119–33.
- [3] Hochhauser AM, Benson JD, Gorse Jr RA, Koehl WJ, Painter LJ, Rippon BH, et al. The effect of aromatics, MTBE, olefins and  $T_{90}$  on mass exhaust emissions from current and older vehicles the auto/oil air quality improvement research program. *SAE Trans* 1991:748–88.
- [4] Mitakos D, Blomberg C, Vandersickel A, Wright Y, Schneider B, Boulouchos K. Ignition delays of different homogeneous fuel-air mixtures in a rapid compression expansion machine and comparison with a 3-stage-ignition model parameterized on shock tube data. *SAE Int J Engines* 2013;6:1934–52.

- [5] Javed T, Nasir EF, Ahmed A, Badra J, Djebbi K, Beshir M, et al. Ignition delay measurements of light naphtha: a fully blended low octane fuel. *Proc Combust Inst* 2017;36:315–22.
- [6] Alabbad M, Issayev G, Badra J, Voice AK, Giri BR, Diebki K, et al. Autoignition of straight-run naphtha: a promising fuel for advanced compression ignition engines. *Combust Flame* 2018;189:337–46.
- [7] Zhong A, Li X, Turányi T, Huang Z, Han D. Pyrolysis and oxidation of a light naphtha fuel and its surrogate blend. *Combust Flame* 2022;240:111979.
- [8] Wang B, Wang Z, Shuai S, Xu H. Combustion and emission characteristics of multiple premixed compression ignition (MPCI) mode fuelled with different low octane gasolines. *Appl Energy* 2015;160:769–76.
- [9] Çelebi S, Duzcan B, Demir U, Uyumaz A, Haşimoğlu C. Effects of light naphtha utilization on engine performance in an homogeneous charged compression ignition engine. *Fuel* 2021;306:121663.
- [10] Lu A, Zhang C, Ren Y, Li Y, Li S, Yin P. Research on knock recognition of coal-based naphtha homogeneous charge compression ignition engine based on combined feature extraction and classification. *Fuel* 2021;300:120997.
- [11] Gallagher SM, Curran HJ, Metcalfe WK, Healy D, Simmie JM, Bourque G. A rapid compression machine study of the oxidation of propane in the negative temperature coefficient regime. *Combust Flame* 2008;153:316–33.
- [12] Mittal G, Sung CJ. Aerodynamics inside a rapid compression machine. *Combust Flame* 2006;145:160–80.
- [13] Bourgeois N, Jeanmart H, Winckelmans G, Lamberts O, Contino F. How to ensure the interpretability of experimental data in rapid compression machines? A method to validate piston crevice designs. *Combust Flame* 2018;198:393–411.
- [14] Bartenev AM, Gelfand BE. Spontaneous initiation of detonations. *Prog Energy Combust* 2000;26:29–55.
- [15] Sharpe GJ, Short M. Detonation ignition from a temperature gradient for a two-step chain-branching kinetics model. *J Fluid Mech* 2003;476:267–92.
- [16] Pan J, Sheppard CGW, Tindall A, Berzins M, Pennington SV, Ware JM. End gas inhomogeneity, autoignition and knock. *SAE Trans* 1998:1748–62.
- [17] Gu XJ, Emerson DR, Bradley D. Modes of reaction front propagation from hot spots. *Combust Flame* 2003;133:63–74.
- [18] Kapila AK, Schwendeman DW, Quirk JJ, Hawa T. Mechanisms of detonation formation due to a temperature gradient. *Combust Theory Model* 2002;6:553.
- [19] Pöschl M, Sattelmayer T. Influence of temperature inhomogeneities on knocking combustion. *Combust Flame* 2008;153:562–73.
- [20] Strozzi C, Mura A, Sotton J, Bellenoù M. Experimental analysis of propagation regimes during the autoignition of a fully premixed methane–air mixture in the presence of temperature inhomogeneities. *Combust Flame* 2012;159:3323–41.
- [21] Pan J, Hu Z, Wei H, Pan M, Liang X, Shu G, et al. Understanding strong knocking mechanism through high-strength optical rapid compression machines. *Combust Flame* 2019;202:1–15.
- [22] Wang Z, Qi Y, He X, Wang J, Shuai S, Law CK. Analysis of pre-ignition to super-knock: hotspot-induced deflagration to detonation. *Fuel* 2015;144:222–7.
- [23] Büttgen RD, Raffius T, Grünefeld G, Koß HJ, Heufer A. High-speed imaging of the ignition of ethanol at engine relevant conditions in a rapid compression machine. *Proc Combust Inst* 2019;37:1471–8.
- [24] Wang Y, Qi Y, Liu W, Wang Z. Investigation of methanol ignition phenomena using a rapid compression machine. *Combust Flame* 2020;211:147–57.
- [25] Liu W, Qi Y, Zhang R, Wang Z. Flame propagation and auto-ignition behavior of iso-octane across the negative temperature coefficient (NTC) region on a rapid compression machine. *Combust Flame* 2022;235:111688.
- [26] Pan J, Zheng Z, Wei H, Zheng Z, Wei H, Pan M, et al. An experimental investigation on pre-ignition phenomena: emphasis on the role of turbulence. *Proc Combust Inst* 2021;38:5801–10.
- [27] Kalghatgi GT, Bradley D, Andrae J, Harrison AJ. The nature of ‘superknock’ and its origins in SI engines. In: IMechE conference on internal combustion engines: performance fuel economy and emissions; 2009. p. 8–9.
- [28] Bates L, Bradley D, Paczko G, Peters N. Engine hot spots: modes of auto-ignition and reaction propagation. *Combust Flame* 2016;166:80–5.
- [29] Xie Y, Lu A, Li J, Yang J, Zhang C, Morsy M. Laminar burning characteristics of coal-based naphtha. *Combust Flame* 2023;249:112625.
- [30] Knop V, Loos M, Pera C, Jeuland N. A linear-by-mole blending rule for octane numbers of n-heptane/iso-octane/toluene mixtures. *Fuel* 2014;115:666–73.
- [31] Mehl M, Pitz WJ, Westbrook CK, Curran H. Kinetic modeling of gasoline surrogate components and mixtures under engine conditions. *Proc Combust Inst* 2011;33:193–200.
- [32] Sarathy SM, Kukkadapu G, Mehl M, Javed T, Ahmed A, Naser N, et al. Compositional effects on the ignition of FACE gasolines. *Combust Flame* 2016;169:171–93.
- [33] CHEMKIN-Pro 19.2. Reaction design. San Diego, California. 2017.
- [34] MATLAB 2021b, The MathWorks Inc., Natick, Massachusetts, 2021.
- [35] Otsu N. A threshold selection method from gray-level histograms. *IEEE Trans Syst Man Cybern* 1979;9:62–6.
- [36] Zeldovich YB. Regime classification of an exothermic reaction with nonuniform initial conditions. *Combust Flame* 1980;39:211–4.
- [37] Michelbach C, Tomlin A. An experimental and kinetic modeling study of the ignition delay and heat release characteristics of a five component gasoline surrogate and its blends with iso-butanol within a rapid compression machine. *Int J Chem Kinet* 2021;53:787–808.
- [38] Gorbatenko I, Tomlin AS, Lawes M, Cracknell RF. Experimental and modelling study of the impacts of n-butanol blending on the auto-ignition behaviour of gasoline and its surrogate at low temperatures. *Proc Combust Inst* 2019;37:501–9.
- [39] Gorbatenko I, Bradley D, Tomlin A. Auto-ignition and detonation of n-butanol and toluene reference fuel blends (TRF). *Combust Flame* 2021;229:111378.
- [40] Ju Y, Reuter CB, Yehia OR, Farouq TI, Won SH. Dynamics of cool flames. *Prog Energy Combust Sci* 2019;75:100787.
- [41] Alabbad M, Javed T, Khaled F, Badra J, Farooq A. Ignition delay time measurements of primary reference fuel blends. *Combust Flame* 2017;178:205–16.
- [42] Mohamed C. Suppression of reaction during rapid compression and its effect on ignition delay. *Combust Flame* 1998;112:438–44.
- [43] Curran HJ, Gaffuri P, Pitz WJ, Westbrook CK. A comprehensive modeling study of n-heptane oxidation. *Combust Flame* 1998;114:149–77.
- [44] Mittal G, Chaos M, Sung CJ, Dryer FL. Dimethyl ether autoignition in a rapid compression machine: experiments and chemical kinetic modeling. *Fuel Process Technol* 2008;89:1244–54.
- [45] Goldsborough SS, Hochgreb S, Vanhove G, Wooldridge MS, Curran HJ, Sung CJ. Advances in rapid compression machine studies of low-and intermediate-temperature autoignition phenomena. *Prog Energy Combust Sci* 2017;63:1–78.
- [46] Bradley D, Lawes M, Materego M. Interpretation of auto-IDTs measured in different rapid compression machines. In: 25th international colloquium on the dynamics of explosions and reactive systems, Leeds; 2015.
- [47] Sung C, Curran H. Using rapid compression machines for chemical kinetics studies. *Prog Energy Combust Sci* 2014;44:1–18.
- [48] Griffiths JF, MacNamara JP, Sheppard CGW, Turton DA, Whitaker BJ. The relationship of knock during controlled autoignition to temperature inhomogeneities and fuel reactivity. *Fuel* 2002;81:2219–25.
- [49] Zhen X, Wang Y, Xu S, Zhu Y, Tao C, Xu T, et al. The engine knock analysis—an overview. *Appl Energy* 2012;92:628–36.
- [50] Robert A, Richard S, Colin O, Poinso T. LES study of deflagration to detonation mechanisms in a downsized spark ignition engine. *Combust Flame* 2015;162:2788–807.
- [51] Morley C. GASEQ: a chemical equilibrium program for Windows. <http://www.gaseq.co.uk>; 2005.
- [52] Lutz AE, Kee RJ, Miller JA, Dwyer HA, Oppenheim AK. Dynamic effects of autoignition centers for hydrogen and C1, 2-hydrocarbon fuels. *Symp Combust* 1988;22:1683–93.
- [53] Lee JH. The detonation phenomenon. Cambridge: Cambridge University Press; 2008.
- [54] Williams FW, Indritz D, Sheinson RS. Concentration limits for n-butane low temperature flames. *Combust Sci Technol* 1975;11:67.
- [55] Hwang W, Dec J, Sjöberg M. Spectroscopic and chemical-kinetic analysis of the phases of HCCI autoignition and combustion for single-and two-stage ignition fuels. *Combust Flame* 2008;154:387–409.